

Supplemental Text and Figures

1. Methods

1.1 Scanning Electron Microscope Methods.....	2
1.2 Electron Microprobe Methods.....	2
1.2.1 Electron Microprobe Mapping.....	2
1.2.2 Electron Microprobe Quantitative Analysis.....	2
1.3 Monazite and Xenotime U-Th-Pb _{total} Geochronology.....	3
1.3.1 Electron Microprobe Mapping of Monazite and Xenotime.....	3
1.3.2 Monazite and Xenotime Quantitative Analysis.....	4
1.4 Thermobarometry Methods.....	5
1.4.1 Internally Consistent Thermobarometry.....	5
1.4.2 Pseudosection Methods.....	7
1.5 U-Pb Zircon Geochronology Methods.....	7
1.6 Whole Rock Geochemistry Methods.....	11
1.6.1 X-ray Fluorescence (XRF) Methods.....	11
1.6.2 Inductively Coupled Plasma-Mass Spectrometry (ICP-MS) Methods.....	12

2. Petrology and Sample Descriptions.....	13
---	----

Supplementary Tables

Table S1: Mineral Compositions Used for Estimation of Metamorphic Conditions.....	6
Table S2: Analytical Method Metadata for LA-ICP-MS U-Pb Geochronology of Zircon.....	9
Table S3: Sample Locations and Descriptions	15
Table S4: Mineral Proportions Determined by the Analyze Phases Function in Aztec 6.0.....	18

Supplementary Figures

Fig. S1: Outcrop and hand sample photos of sample 21IWH05.....	23
Fig. S2: Outcrop and hand sample photos of sample 21IWH07.....	24
Fig. S3: Outcrop photos of sample 21IWH11.....	25
Fig. S4: Photos of drill core sample 21IWH18.....	26
Fig. S5: Outcrop photos of samples 21AG06 and 21IWH04.....	27
Fig. S6: Outcrop photos of samples 21IWH03 and 21IWH06.....	28
Fig. S7: Full thin section scans of igneous rock samples.....	29
Fig. S8: Full thin section scans of metamorphic rock samples.....	30
Fig. S9: Photomicrographs from sample 21IWH05.....	31
Fig. S10: Photomicrographs from sample 21IWH07.....	32
Fig. S11: Photomicrographs of sample 21IWH11.....	36
Fig. S12: Photomicrographs of sample 21IWH18.....	37
Fig. S13: Full thin section EDS compositional maps for sample 21IWH05.....	38
Fig. S14: Full thin section EDS compositional maps for sample 21IWH07.....	39
Fig. S15: Full thin section EDS compositional maps for samples 21IWH11A and 21IWH11B.....	40
Fig. S16: Full thin section EDS compositional maps for drill core sample 21IWH18.....	41
Fig. S17: Full thin section phase maps of samples 21IWH05, 21IWH07, 21IWH11A, and 21IWH18.....	42
Fig. S18: Monazite and xenotime locations for samples 21IWH05 and 21IWH07.....	43
Fig. S19: Monazite and xenotime locations for samples 21IWH11A and 21IWH11B.....	44
Fig. S20: Monazite and xenotime locations for sample 21IWH18.....	45
Fig. S21: Y, Th, Nd, Ca, and U maps of dated monazite grains.....	46
Fig. S22: Backscattered electron images of xenotime grains in sample 21IWH11.....	51
Fig. S23: Yb, U, Th, Dy, Gd maps of dated xenotime grains.....	54
Fig. S24: Garnet maps and transects from 21IWH07.....	55
Fig. S25: Garnet maps and transects from sample 21IWH18.....	55
Fig. S26: Monazite dates vs composition.....	56
Fig. S27: Xenotime dates vs composition.....	57
Fig. S28: Isochemical phase diagram (pseudosection) for sample 21IWH07.....	58
Fig. S29: Isochemical phase diagram (pseudosection) for sample 21IWH18.....	59
Fig. S30: Cathodoluminescence (CL) images for zircon grains from sample 21AG06.....	60
Fig. S31: Cathodoluminescence (CL) images for zircon grains from sample 21IWH03.....	61
Fig. S32: Cathodoluminescence (CL) images for zircon grains from sample 21IWH04.....	62
Fig. S33: Cathodoluminescence (CL) images for zircon grains from sample 21IWH06.....	63

Supplementary material

The supplementary text contains additional description of samples and samples localities, and detailed descriptions of analytical methods. Minerals abbreviations in the text, tables and figures follow those suggested by Whitney and Evans (2010). Zircon, monazite, and xenotime geochronologic data, whole rock geochemical data, and silicate quantitative analytical results are tabulated in an associated spreadsheet. Data are sorted into tabs by method.

1. Methods

1.1 Scanning Electron Microscope Methods

Entire polished thin sections were using EDS mapped using SEM. Maps were collected with 20 kV beam conditions, a spot size of 5 μm , a working distance of 12 mm, and 100x magnification. Full thin section maps, corrected for background interferences, of major (Al, Si, Mg, Na, K, etc) and minor/trace (P, Y, Ce, Zr) elements and phases were created in Aztec EDS 6.0 software.

1.2 Electron Microprobe Methods

1.2.1 Electron Microprobe Mapping

High resolution compositional maps of silicate (garnet, plagioclase) and phosphate (monazite, xenotime) phases were created using the fully automated JEOL JXA-8900 electron microprobe equipped with five wavelength X-ray spectrometers. Stage X-ray maps of garnet for Ca, Mg, Fe, Mn, and Y were acquired at 15 kV and 150 nA using a slightly defocused beam, 2-20 μm step step (depending on grain size), and 50 ms dwell time. These maps, along with full section EDS maps and thin section scans, were used to guide quantitative analyses.

1.2.2 Electron Microprobe Quantitative Analysis

Quantitative major element compositional traverses were measured with the JEOL JXA-8900 electron microprobe for garnet, amphibole, plagioclase, muscovite, and biotite. We avoided highly altered grains/domains and targeted grains with the largest compositional variability. Muscovite and biotite were analyzed at a variety of distances from garnet. Traverses were collected at 15 kV, 20 nA, and 40° takeoff angle with a focused beam for garnet and a defocused (5 µm) beam for amphibole, feldspar, muscovite, and biotite. Count times were 20 counts/s on peak and 10 counts/s on background. Uncertainties are estimated at <1% for major elements and approximately ±3% for minor elements based upon repeated analysis of standard materials (Lowers and Meeker, 2004; Swayze et al., 2018). Calibrations were made using common natural and synthetic standards (see also Swayze et al., 2018). Standards utilized are as follows: muscovite, biotite, & garnet: Ca & Si: Wollastonite GKC-03; Sr: Strontium Silicate; F: CaF₂; K: orthoclase; Cl: sodalite; Fe: Synthetic Fayalite; Mn: spessartine; Cr: MgCrO₄ (synthetic); Ba: barite; Ti: rutile; Na: Tiburon Albite; Al: Miyake Anorthite; Mg: Wakefield Diopside. Plagioclase: Si & Al: Miyake Anorthite; Sr: Strontium silicate; K: orthoclase; Cl: sodalite; Fe: Synthetic Fayalite; Mn: spessartine; Ba: barite; Na: Tiburon Albite; Mg: Spring Water Olivine. Amphibole: Si, Ca, & Mg: Wakefield Diopside; Sr: Strontium silicate; F: CaF₂; K: orthoclase; Cl: sodalite; Fe: synthetic fayalite; Mn: spessartine; Cr: MgCrO₄ (synthetic); Ba: barite; Ti: rutile; Na: Tiburon Albite; Al: Miyake Anorthite. Chemical formulae were calculated stoichiometrically based on 12 oxygens for garnet, 8 oxygens for plagioclase and K-feldspar, and 22 oxygens for biotite, muscovite, and amphibole.

1.3 Monazite and Xenotime U-Th-Pb_{total} Geochronology

1.3.1 Electron Microprobe Mapping of Monazite and Xenotime

Monazite and xenotime maps were acquired with the fully automated JEOL JXA-8900 electron microprobe equipped with five wavelength X-ray spectrometers housed. Operating conditions were 200 nA and 15 kV, with a focused beam and 100 ms dwell time. WDS maps for monazite grains were collected for Th, U, Y, Ca, and Nd. Xenotime grains were mapped for Yb, Dy, Gd, Th, and U. Maps were simultaneously processed in Adobe Photoshop CC following methods of Williams et al. (2006, 2007, 2017).

1.3.2 Monazite and Xenotime Quantitative Analysis

Examination of high-resolution monazite and xenotime compositional maps were used to develop an analytical strategy for each sample and grain. Individual compositional domains were sampled (dated) with preference given to grains with multiple compositional domains as the geometric constraint of core-to-rim growth directly constrains the relative age of the domains.

Monazite and xenotime were analyzed for major and trace element composition and U-Th-Pb_{total} dating on the Cameca SX100 Ultrachron electron microprobe at the University of Massachusetts Amherst which is uniquely designed for geochronologic analysis. Analytical methods largely followed those of Williams et al. (2006, 2007, 2017) and Hetherington et al. (2008). Five spectrometers were used for measuring U, Th, Pb, S, Ca, K, Sr, Si, Y, P, and rare earth elements (REE). For each compositional domain, a single background analysis is made using the multi-point method of Allaz et al. (2019). Then, four to eight “peak” measurements are made within the same compositional domain immediately adjacent to the background spot. A single date is calculated for each domain based on one background intensity and the peak analyses. Measurements were excluded from the date calculation when compositions were significantly outside the mean for the particular compositional domain, and when the values suggest overlap with adjacent domains of differing composition (Regan et al. 2014). Uncertainty

is determined through propagation of the measurement and background errors through the age equation of Montel et al. (1996). Weighted means of monazite and xenotime populations, as determined by compositional and microstructural analysis, were determined in IsoplotR (Vermeesch, 2018).

Calibration for monazite analyses was performed on natural and synthetic standards. PbPO_4 (pyromorphite) was used for Pb, ThPO_4 (barbanite) was used for Th, and UO_2 was used for U. Moacyr and GSC6413 were used as consistency standards for monazite and xenotime, respectively. These standards are described in Dumond et al. (2008) and Hetherington et al. (2008). Moacyr has an established $^{207}\text{Pb}/^{235}\text{U}$ date by isotope dilution-thermal ionization mass spectrometry (ID-TIMS) analysis of 504.3 ± 0.2 Ma (Gasquet et al., 2010). GSC6413 yielded $^{206}\text{Pb}/^{238}\text{U}$ and $^{207}\text{Pb}/^{206}\text{Pb}$ ID-TIMS dates of 993.8 ± 0.7 Ma and 996.7 ± 0.8 Ma, respectively (Stern and Rayner, 2003). A second independent set of ID-TIMS analyses from 7 fragments of GSC6413 yielded $^{206}\text{Pb}/^{238}\text{U}$ and $^{207}\text{Pb}/^{206}\text{Pb}$ dates of $997 \pm 0.2/0.3/1.3$ Ma and $999.7 \pm 0.3/5.0$ Ma, respectively (Schoene et al., 2006) where $\pm X/Y/Z$, X is the analytical uncertainty, Y includes the analytical and tracer contributions, and Z includes the analytical, tracer and decay constant uncertainties. Heatherington et al. (2008) determined a U-Th-Pb_{total} date of 1000 ± 8 Ma via electron microprobe for GSC6413. Calibration was carried out prior to each analytical session and checked and updated throughout the session as required.

1.4 Thermobarometry Methods

1.4.1 Internally Consistent Thermobarometry

Internally consistent thermobarometry was carried out using winTWQ (Berman, 1991, 2007) in 64-bit mode. The most recent version of the thermodynamic database, DEC06.DAT, was utilized in TWQ version 2.32. Details of this database are described in Berman (2007). The

solution models employed are from winTWQ file DEC06.SLN. The specific activity models used were Berman and Aranovich (2007) for garnet and biotite, Fuhrman and Lindsley (1988) for plagioclase, and Chatterjee and Froese (1975) for white mica. The specific compositions input into TWQ are summarized in Table S1. Thermobarometric calculations were applied to minerals from the same metamorphic fabric that appeared to be in equilibrium.

Table S1. Mineral compositions used for estimation of metamorphic conditions.

Sample	21IWH07			21IWH18				21IWH05	
Mineral	Grt	Pl	Bt	Grt	Pl	Bt	Ms	Ms	Bt
SiO ₂	35.87	67.84	34.51	37.26	64.04	34.85	44.99	44.64	36.97
TiO ₂	-	-	1.83	-	-	2.01	0.30	0.38	1.15
Al ₂ O ₃	20.27	20.95	18.72	21.36	23.44	16.86	30.95	31.67	19.03
FeO	37.42	0.02	21.25	30.99	0.05	22.28	4.49	4.34	10.05
MnO	0.84	-	0.16	1.94	-	0.48	0.02	0.06	1.50
MgO	2.77	-	8.48	4.04	-	8.25	1.22	1.55	15.97
CaO	0.89	1.88	0.04	1.47	0.93	0.02	-	0.10	0.11
Na ₂ O	-	10.73	0.10	-	9.36	0.05	0.16	0.36	0.18
K ₂ O	-	0.06	9.61	-	1.11	9.85	11.12	10.47	8.88
X _{Alm}	0.8396	-	-	0.7312	-	-	-	-	-
X _{Sps}	0.0197	-	-	0.0477	-	-	-	-	-
X _{Grs}	0.0264	-	-	0.0459	-	-	-	-	-
X _{Py}	0.1143	-	-	0.1751	-	-	-	-	-
X _{An}	-	0.0881	-	-	0.2073	-	-	-	-
X _{Ab}	-	0.9084	-	-	0.7822	-	-	-	-
X _{Or}	-	0.0035	-	-	0.105	-	-	-	-

1.4.2 Pseudosection Methods

GeoPS v. 3.3 (Xiang and Connolly, 2022) was used to calculate isochemical phase diagrams (pseudosections) using the internally consistent thermodynamic dataset of Holland and Powell (2011) in the model system $\text{MnO-Na}_2\text{O-MgO-Al}_2\text{O}_3\text{-SiO}_2\text{-K}_2\text{O-CaO-FeO-TiO}_2\text{-H}_2\text{O}$ (MnNCKFMASHTO). Fe^{3+} was not considered as there were no Fe^{3+} -rich oxides observed in the modeled samples (21IWH07 and 21IWH18). We utilized the activity-composition models rmetapelite dataset (Holland and Powell 2011; Green et al. 2016) and activity-solution models for equilibria in metapelitic bulk compositions: biotite, garnet, and muscovite from White et al. (2014a), ilmenite from White et al. (2000; 2007) and ternary feldspar (Fuhrman and Lindsley, 1988). Calculations with the metapelite models were extended by White et al. (2014b) to include MnO and spessartine. Fluid was considered with the model of Holland and Powell (1998). This set of activity-solution models was employed for its compatibility with the examined bulk compositions and internally consistent thermodynamic dataset of Holland and Powell (2011). The bulk composition was calculated from the adapted XRF/ICP-MS composition from the rock determined at the Washington State University Peter Hooper Geoanalytical lab (see section 1.6). Water content was estimated from the bulk rock loss on ignition (LOI) values. Pseudosections were calculated under water saturated conditions for samples equilibrated under subsolidus conditions ($a_{\text{H}_2\text{O}}=1$), and with water as a component for suprasolidus samples (Mottram et al. 2014). Additional details and information are provided on the raw GeoPS output plots shown on Figures S28 and S29.

1.5 U-Pb Zircon Geochronology Methods

U-Pb analyses of zircon were made using a Nu Plasma AttoM magnetic sector inductively coupled plasma mass spectrometer (ICP-MS) coupled to an ESI NWR 193UC laser

ablation (LA) system consisting of a TwoVol2 ablation chamber and a Coherent Excistar 193 nm ArF excimer laser. Zircons were hand-picked from the non-magnetic fraction, mounted in a twenty-five millimeter epoxy grain mount and polished to center. A 15 μm laser spot was used for all analyses and placed on regions of zircon grains free of fractures, inclusions, or overgrowths, guided by CL images. Careful imaging of the zircon grains both in transmitted and reflected light prior to laser ablation allowed the choice of laser spot size and positioning to be made most effectively. The locations of LA-ICP-MS spot analyses are overlain on cathodoluminescence images are shown on Figures S30-33.

Analytical details and instrument parameters are included in Table S2. Zircon 91500 (Wiedenbeck et al. 2004) was used to correct for mass spectrometer bias on Pb/Pb and U-Pb isotopic ratios and downhole U/Pb fractionation (Kosler et al. 2002) and calculate U and Th concentrations from background-corrected count rates. Pb/Pb and U/Pb isotopic dates and U and Th concentrations were determined using Iolite software (v.4) and the U-Pb geochronology data reduction scheme (Paton et al. 2010). No common Pb correction was made to the final data. U-Pb zircon data for unknown samples are listed in the supplementary dataset. Only single analyses between 2-3 % concordant (for both U-Pb and Pb-Pb dates) with approximately 5 seconds of data were used for final date calculations.

Five zircon secondary reference materials (SRMs) were analyzed with the zircons separated from the Needles Mountain as a check and monitor on data quality: 94-35 zircon (55.5 ± 1.5 Ma (2s); Klepeis et al (1998); Plesovice zircon (337.16 ± 0.11 Ma (2s); Slama et al. 2008, recalculated by Horstwood et al. 2016); R33 zircon (419.3 ± 0.4 Ma (2s); Black et al. 2004); QGNQ zircon (1851.6 ± 0.6 Ma (2s); Black et al. 2004); and (Tan Brown zircon (2512.24 ± 0.71 Ma (2s); Bauer et al. 2020). U-Pb zircon data for the SRMs analyzed with Needles Mountains,

CO zircon grain unknowns are listed in the supplementary dataset and calculated concordia ages for SRMSs are reported in Table S2.

Table S2. Analytical method metadata for LA-ICP-MS U-Pb geochronology of zircon

Laboratory and Sample Preparation	
Laboratory name	Mineral Isotope Laser Laboratory (MILL), Texas Tech University
Sample type/mineral	Zircon
Sample preparation	<i>Electro Pulse Dissagregator (EPD)</i> , water table, and heavy liquid mineral separation; hand pick; 25-mm epoxy resin mount; 1-mm polish to finish
Scanning Electron Microscope (SEM) Imaging	Cathodoluminescence (CL) imaging: JEOL 5800 LV SEM
Laser ablation system	
Make, Model and type	ESI/New Wave Research, NWR193UC ArF excimer laser
Ablation cell	TwoVol2 two-volume ablation chamber
Laser wavelength (nm)	193 nm
Pulse width (ns)	5 ns
Fluence (J cm^{-2})	3 J cm^{-2}
Repetition rate (Hz)	8 Hz
Ablation duration (s)	30 s
Spot diameter (μm) nominal/actual	15 μm
Sampling mode / pattern	Static spot ablation
Carrier gas	100% He in the cell, Ar make-up gas combined using a Y- piece 75% along the sample transport line to the torch.
Cell carrier gas flow (He, l min^{-1})	$0.81 - 0.82 \text{ l min}^{-1}$
ICP-MS Instrument	
Make, Model and type	Nu Instruments, Nu AttoM ICP-MS
Sample introduction	Laser Ablation
RF power (W)	1300 W
Ar gas flows (l min^{-1})	Cool gas (Ar) = 13.0 l min^{-1} Aux gas (Ar) = 0.86 l min^{-1} Ar make gas (Ar) = 0.68 l min^{-1}

Detection system	MasCom Electron Multiplier
Masses measured	202, 204, 206, 207, 208, 232, 235, 238
Integration time per peak/dwell times (ms)	200 μ s for each isotope except 400 μ s 206, 1ms 207, 2ms 235
Total integration time per output data point (s)	0.1984 s
Analysis mode/ Detection mode	Deflector jump/Pulse counting
IC Dead time (ns)	9.2 ns
Data Processing	
Calibration strategy	91500 zircon used as primary reference material, Plešovice, Tan Brown, R33, 9980, and Fish Canyon Tuff zircons used as secondaries/validation
Reference material (zircon) information	91500 (Wiedenbeck et al. 1995) Plešovice (Sláma et al. 2008) Tan Brown (Bauer et al. 2020) R33 (Black et al. 2004) QGNG (Black et al. 2004) 94-35 (Klepeis et al. 1998)
Data processing package used / Correction for LIEF	Iolite (v4) and VizualAge DRS (Petrus and Kamber 2012) software for data normalization, uncertainty propagation and age calculation. LIEF correction modeled using Exponential model in Iolite for 91500 zircon. Assumes reference material and samples behave identically. Ages are quoted at 2s absolute.
Common-Pb correction, composition and uncertainty	No common-Pb correction applied to data
Quality control / Validation / Concordia Ages	Plešovice (Concordia age): 338.9 ± 3.2 (2s, MSWD = 0.10, n = 15) Tan Brown (Concordia age): 2512 ± 5 (2s, MSWD = 0.19, n = 14) R33 (Concordia age): 413.9 ± 5.1 (2s, MSWD = 0.14, n = 15) QGNG (Concordia age): 1852.03 ± 11.3 (2s, MSWD = 0.11, n = 16) 94-35 (Concordia age): 55.68 ± 0.52 (2s, MSWD=0.12, n=13)

1.6 Whole Rock Geochemistry Methods

1.6.1 X-ray Fluorescence (XRF) Methods

Major and minor elements were determined by XRF at the Washington State University Peter Hooper Geoanalytical lab. Analytical methods are summarized from <https://environment.wsu.edu/facilities/geoanalytical-lab/technical-notes/xrf-method/>.

Fresh chips of the sample were hand picked and a standard volume of chips (approximately 28 g) is ground in a swing mill with tungsten carbide surfaces for 2 minutes. Three and a half grams (3.5 g) of the sample powder were weighed into a plastic mixing jar with 7.0 g of spec pure dilithium tetraborate ($\text{Li}_2\text{B}_4\text{O}_7$) and, assisted by an enclosed plastic ball, mixed for ten minutes. The mixed powders were emptied into graphite crucibles with internal measurements of 34.9 mm diameter by 31.8 mm deep. Twenty four (24) filled crucibles were placed on a silica tray and loaded into a muffle furnace only large enough to contain the tray. Fusion takes 5 minutes from the time the preheated furnace returned to its normal 1000°C after loading. The silica plate and graphite crucibles were then removed from the oven and allowed to cool. Each bead is reground in the swing mill for 35 seconds, the glass powder then replaced in the graphite crucibles and refused for 5 minutes.

Following the second fusion, the cooled beads were labeled with an engraver, their lower flat surface was ground on 600 silicon carbide grit, finished briefly on a glass plate (600 grit with alcohol) to remove any metal from the grinding wheel, washed in an ultrasonic cleaner, rinsed in alcohol and wiped dry. The glass beads were then ready to be loaded into the XRF spectrometer.

The concentrations of 27 elements in the unknown samples were measured by comparing the X-ray intensity for each element with the intensity for two beads each of nine

USGS standard samples (PCC-1, BCR-1, BIR-1, DNC-1, W-2, AGV-1, GSP-1, G-2, and STM -1) and two beads of pure vein quartz used as blanks for all elements except Si. The 20 standard beads were run and used for recalibration approximately once every three weeks or after the analysis of about 300 unknowns. The intensities for all elements were corrected automatically for line interference and absorption effects due to all the other elements using the fundamental parameter method.

1.6.2 Inductively Coupled Plasma-Mass spectrometry (ICP-MS) Methods

Trace elements were determined by inductively coupled plasma-mass spectrometry ICP-MS at the Washington State University Peter Hooper Geoanalytical lab using methods summarized from <https://environment.wsu.edu/facilities/geoanalytical-lab/technical-notes/icp-ms-method/>.

The flux used for the fusion was di-Lithium-tetraborate (Spectromelt® A-10, EM Science, Gibbstown, NJ). Reagents are HNO₃ 69-70% (Fisher ACS plus grade), HF 48-52% (Baker ACS reagent grade), HClO₄ 67-71% (Fisher Trace Metal Grade), and H₂O₂ (Baker ACS Reagent). The HF was further purified before use by sub-boiling distillation in a teflon still. All water used is >18 M deionized water from a Nanopure water system.

Powdered samples were mixed with an equal amount of lithium tetraborate flux (typically 2g), placed in a carbon crucible and fused at 1000° C in a muffle furnace for 30 minutes. After cooling, the resultant fusion bead was briefly ground in a carbon-steel ring mill and a 250 mg portion is weighed into a 30 ml, screw-top Teflon PFA vial for dissolution. The acid dissolution consists of a first evaporation with HNO₃ (2 ml), HF (6 ml), and HClO₄ (2 ml) at 110° C. After evaporating to dryness, the sample was wetted and the sides of the vial were rinsed with a small amount of water before a second evaporation with HClO₄ (2 ml) at

160° C. After the second evaporation, samples were brought into solution by adding approximately 10 ml of water, 3 ml HNO₃, 5 drops H₂O₂, 2 drops of HF and warmed on a hot plate until a clear solution is obtained. The sample was then transferred to a clean 60 ml HDPE bottle diluted up to a final weight of 60g with de-ionized water.

Solutions are analyzed on an Agilent model 4500 ICP-MS and were diluted an additional 10X at the time of analysis using Agilent's Integrated Sample Introduction System (ISIS). This yielded a final dilution factor of 1:4800 relative to the amount of sample fused. Instrumental drift was corrected using Ru, In, and Re as internal standards. Internal standardization for the REEs used a linear interpolation between In and Re to compensate for mass-dependant differences in the rate and degree of instrumental drift. Isobaric interference of light rare earth oxides on the mid- heavy REEs can be a significant source of error in ICP-MS analysis, so tuning was optimized to keep the CeO/Ce ratio below 0.5%. Correction factors used to compensate for the remaining oxide interferences were estimated using two mixed-element solutions. The first contained Ba, Pr, and Nd, and the second Tb, Sm, Eu, and Gd. Standardization was accomplished by processing duplicates of three in-house rock standards interspersed within each batch of 18 unknowns. Concentrations, oxide- and drift corrections were then calculated offline using a spreadsheet. Long term precision for the method is typically better than 5% (RSD) for the REEs and 10% for the remaining trace elements.

2. Petrology and Sample Descriptions

Detailed descriptions of all samples and sample locations that formed part of this study are summarized in Table S3. Mineral proportions calculated in Aztec EDS software are summarized in Table S4. Further sample characterization is provided in the supplementary

figures. Photos of sample localities are provided for all samples: 21IWH05 (Fig. S1), 21IWH07 (Fig. S2), 21IWH11 (Fig. S3), 21IWH18 (Fig. S4), 21AG06 (Fig. S5A-B), 21IWH04 (Fig. S5C-D), 21IWH03B (Fig. S6A-B), and 21IWH06 (Fig. S6C-D). Full thin section plane (PPL) and cross polarized (XPL) photomicrographs of samples 21AG06, 21IWH04, 21IWH03B, and 21IWH06 are provided on Figure S7. Full thin section plane (PPL) and cross polarized (XPL) photomicrographs of samples 21IWH05, 21IWH07, 21IWH11, and 21IWH18 are shown on Figure S8. Select photomicrographs highlighting key phase relationships are provided for samples 21IWH05 (Fig. S9), 21IWH07 (Fig. S10), 21IWH11 (Fig. S11), and 21IWH18 (Fig. S12). Full thin sections EDS compositional maps of samples 21IWH05 (Fig. S13), 21IWH07 (Fig. S14), 21IWH11 (Fig. S15), and 21IWH18 (Fig. S16). Full thin sections phase maps of samples 21IWH05, 21IWH07, 21IWH11, and 21IWH18 are provided on Figure S17. Full thin section backscattered electron (BSE) images overlain with the location of monazite and xenotime grains are provided for samples 21IWH05 (Fig. S18A), 21IWH07 (Fig. S18B), 21IWH11A (Fig. S19A), 21IWH11B (Fig. S19B), and 21IWH18 (Fig. S20). Electron microprobe maps of Y, Th, U, Ca, and Nd in monazite are provided for dated grains in sample 21IWH05 (Fig. S21A), 21IWH07 (Fig. S21B), 21IWH11A (Fig. S21C), 21IWH11B (Fig. 21D), and 21IWH18 (Fig. S21E). Backscattered electron (BSE) images of dated xenotime in sample 21IWH11A and 21IWH11B are provided in Fig. S22. X-ray compositional maps of dated xenotime in samples 21IWH07 and 21IWH18 are shown in Figure S23. Figure S24 shows garnet X-ray compositional maps and quantitative transects from sample 21IWH07. Figure S25 shows garnet X-ray compositional maps and quantitative transects from sample 21IWH18.

Table S3. Sample locations and descriptions

Sample	Locality	Lat (°N)	Long (°W)	Unit	Description
<i>Igneous samples</i>					
21AG06	Cataract Gulch	38.018918	107.345372	granite of Cataract Gulch	Coarse-grained K-feldspar+plagioclase+quartz+biotite granite. Biotite and feldspar locally altered to chlorite and sericite, respectively. No fabric observed in outcrop. In thin section some feldspar grains are very weakly aligned.
21IWH03	Shore of Electra Lake	37.565707	107.811341	Twilight Gneiss	Fine-grained gneiss with strong fabric defined by biotite. Inter-layered with hornblende-rich gneiss. Alignment of biotite grains define strong foliation in outcrop and thin section. Assemblage includes quartz+plagioclase+K-feldspar+biotite
21IWH04	Bank of small stream near Bakers Bridge	37.459009	107.800547	Bakers Bridge Granite	Coarse-grained K-feldspar+plagioclase+quartz+hornblende+biotite granite. In thin section sample displays fractures/veins and hornblende and feldspar are altered. No fabric visible at outcrop or thin section scale. Alteration of hornblende grains, unlikely to preserve primary compositions, did not permit quantitative thermobarometry.
21IWH06	Float, Vallecito Campground, southern Needle Mountains	37.478508	107.548103	Eolus Granite	Medium-grained K-feldspar+plagioclase (An ₂₇)+hornblende+biotite granodiorite. Weak fabric visible in thin section defined by layered of feldspar, biotite, and hornblende.

Sample	Locality	Lat (°N)	Long (°W)	Unit	Description
<i>Metamorphic samples</i>					
21IWH05	Cliff west of Vallecito Campground, southern Needle Mountains	37.47851	107.548103	Vallecito Conglomerate	Fine- to medium-grained mica-rich quartzite, Schistose foliation defined by muscovite and biotite. Peak assemblage includes: quartz, muscovite, biotite, plagioclase, ilmenite
21IWH07	Potato Hill, just SE of Coal Bank Pass, western Needle Mountains	37.692551	107.769468	Paleoproterozoic gneiss of Needle Mountains (felsic metavolcanic of the Iring Formation?)	Medium-grained felsic gneiss. Peak assemblage forms foliation with schistose/gneissic foliation largely defined by biotite. Phases associated with early foliation include garnet, plagioclase (An ₁₂₋₁₁), biotite, rutile, staurolite. Later foliation largely defined by biotite which deforms earlier (peak) fabric. Staurolite overgrows garnet locally. Staurolite grains largely pseudomorphed to chlorite/white mica. Biotite locally altered to chlorite. Garnet retrograded to biotite/chlorite. Reaction rims near resorbed garnet include high Y monazite+xenotime Peak assemblage includes: quartz, plagioclase, biotite, garnet, staurolite, rutile
21IWH11	Uncompahgre Gorge, south of Ouray, CO	38.014299	107.66754	Uncompahgre Formation	Medium- to coarse-grained, purple to pink, cross bedded quartzite (meta-quartz arenite). Axial-planar cleavage prominent in outcrop.
21IWH18	Drill core PVTG-32015, 443-444 m depth	37.2485	107.0096	N/A	Fine-grained biotite rich paragneiss with strong fabric largely defined by alignment of biotite and

					<p>plagioclase (An₆₀₋₇₃). Small garnet porphyroblasts (200-450 µm) are locally abundant. Rims of (variably chloritized) biotite occur around many garnet grains suggesting retrograde resorption of garnet. Areas around resorbed garnet commonly include relatively high Yb xenotime and relatively high Y monazite. Matrix monazite grains commonly altered to apatite and Th- or REE-bearing phases (e.g. thorite, thorianite), with some core domains locally preserved. White mica locally present in upper left corner of thin section. White mica is in places aligned with biotite that defines main fabric. Zircon is present as trace phase, very small and clear grains.</p> <p>Peak assemblages includes: plagioclase, quartz, biotite, K-feldspar, garnet, melt, (± white mica).</p>
--	--	--	--	--	---

Table S4. Mineral proportions determined by the analyze phases function in Aztec 6.0.

	21IWH05	21IWH07	21IWH11A	21IWH11B	21IWH18
Quartz	71.54	32.16	99.94	99.34	35.93
Plagioclase	2.61	33.41	-	-	36.24
Biotite	6.59	10.28	-	-	13.14
White mica	14.71	-	-	-	5.64
K-feldspar	-	0.09	-	-	1.01
Garnet	-	11.36*	-	-	0.34
Apatite	0.03	0.01	0.01	trace	0.04
Rutile	-	0.01	-	-	-
Xenotime	0.01	trace	trace	trace	0.01
Monazite	0.01	trace	trace	trace	0.01
Zircon	0.01	trace	0.01	0.01	-
Ilmenite	0.1	-	0.01	0.42	-
Magnetite	0.90	-	0.02	0.02	-
Staurolite	-	0.05	-	-	-

*Likely overestimate due to Aztec software's difficulty in differentiating between garnet and some adjacent retrograde phases (e.g. mica).

Note

Any use of trade, firm, or product names is for descriptive purposes only and does not imply endorsement by the U.S. Government.

References in supplementary material

- Allaz, J.M., Williams, M.L., Jercinovic, M.J., Goemann, K., and Donovan, J., 2019, Multipoint background analysis: Gaining precision and accuracy in microprobe trace element analysis: *Microscopy and Microanalysis*, v. 25, p. 30–46, doi:10.1017/S1431927618015660.
- Bauer A.M., Vervoort J.D. and Fisher C.M., 2020. Unraveling the complexity of zircons from the 4.0-2.9 Ga Acasta Gneiss Complex. *Geochimica et Cosmochimica Acta*, v. 283, p. 85–102. <https://doi.org/10.1016/j.gca.2020.05.023>
- Berman, R.G., 1991, Thermobarometry using multi-equilibrium calculations; a new technique, with petrological applications: *The Canadian Mineralogist*, v. 29, p. 833–855.
- Berman, R.G., 2007, winTWQ (version 2.3): a software package for performing internally-consistent thermobarometric calculations: Geological Survey of Canada, Open File, v. 5462, p. 1–41.
- Berman, R.G., Aranovich, L.Ya., Rancourt, D.G., and Mercier, P.H.J., 2007, Reversed phase equilibrium constraints on the stability of Mg-Fe-Al biotite: *American Mineralogist*, v. 92, p. 139–150, doi:10.2138/am.2007.2051.
- Black L.P., Kamo S.L., Allen C.M., Davis D.W., Aleinikoff J.N., Valley J.W. Mundil, R. Campbell I.H., Korsch R.J., Williams I.S., and Foudoulis C., 2004. Improved $^{206}\text{Pb}/^{238}\text{U}$ microprobe geochronology by the monitoring of a trace-element-related matrix effect; SHRIMP, ID-TIMS, ELA-ICP-MS and oxygen isotope documentation for a series of zircon standards. *Chemical Geology*, v. 205(1-2), p. 115–140. <https://doi.org/10.1016/j.chemgeo.2004.01.003>
- Chatterjee, N.D., and Froese, E., 1975, A thermodynamic study of the pseudobinary join muscovite-paragonite in the system $\text{KAlSi}_3\text{O}_8\text{-NaAlSi}_3\text{O}_8\text{-Al}_2\text{O}_3\text{-SiO}_2\text{-H}_2\text{O}$: *American Mineralogist*, v. 60, p. 985–993.
- Dumond, G., McLean, N., Williams, M.L., Jercinovic, M.J., and Bowring, S.A., 2008, High-resolution dating of granite petrogenesis and deformation in a lower crustal shear zone: Athabasca granulite terrane, western Canadian Shield: *Chemical Geology*, v. 254, p. 175–196, doi:10.1016/j.chemgeo.2008.04.014.
- Fuhrman, M.L., and Lindsley, D.H., 1988, Ternary-feldspar modeling and thermometry: *American Mineralogist*, v. 73, p. 201–215.
- Gasquet, D., Bertrand, J.M., Paquette, J.L., Lehmann, J., Ratzov, G., Ascensão De Guedes, R.A., Tiepolo, M., Boullier, A.M., Scaillet, S., and Nomade, S., 2010, Miocene to Messinian deformation and hydrothermal activity in a pre-Alpine basement massif of the French western Alps: New U-Th-Pb and argon ages from the Lauzière massif: *Bulletin de la Societe Geologique de France*, v. 181, p. 227–241, doi:10.2113/gssgfbull.181.3.227.

- Green, E.C.R., White, R.W., Diener, J.F.A., Powell, R., Holland, T.J.B., and Palin, R.M., 2016, Activity–composition relations for the calculation of partial melting equilibria in metabasic rocks: *Journal of Metamorphic Geology*, v. 34, p. 845–869, doi:10.1111/jmg.12211.
- Hetherington, C.J., Jercinovic, M.J., Williams, M.L., and Mahan, K., 2008, Understanding geologic processes with xenotime: Composition, chronology, and a protocol for electron probe microanalysis: *Chemical Geology*, v. 254, p. 133–147, doi:10.1016/j.chemgeo.2008.05.020.
- Holland, T.J.B., and Powell, R., 2011, An improved and extended internally consistent thermodynamic dataset for phases of petrological interest, involving a new equation of state for solids: *Journal of Metamorphic Geology*, v. 29, p. 333–383, doi:10.1111/j.1525-1314.2010.00923.x.
- Holland, T.J.B., and Powell, R., 1998, An internally consistent thermodynamic data set for phases of petrological interest: *Journal of Metamorphic Geology*, v. 16, p. 309–343, doi:10.1111/j.1525-1314.1998.00140.x.
- Horstwood M. S. A., Košler J., Gehrels G., Jackson S. E., McLean N. M., Paton C., Pearson N. J., Sircombe K., Sylvester P., Vermeesch P., Bowring J. F., Condon D. J., and Schoene B., 2016. Community-derived standards for LA-ICP-MS U-(Th-) Pb geochronology—Uncertainty propagation, age interpretation and data reporting. *Geostandards and Geoanalytical Research*, v. 40, p. 311–332. <https://doi.org/10.1111/j.1751-908X.2016.00379.x>
- Klepeis K., Crawford M.L., Gehrels G., 1998. Structural history of the crustal-scale Coast shear zone north of Portland Canal, southeast Alaska and British Columbia: *Journal of Structural Geology*, v. 20, p.883-904.
- Košler J., Fonneland H., Sylvester P., Tubrett M., and Pedersen R.B., 2002, U–Pb dating of detrital zircons for sediment provenance studies—a comparison of laser ablation ICPMS and SIMS techniques: *Chemical Geology*, v. 182, p. 605-618, [https://doi.org/10.1016/S0009-2541\(01\)00341-2](https://doi.org/10.1016/S0009-2541(01)00341-2).
- Lowers, H.A., and Meeker, G.P., 2004, Electron probe microanalysis as a tool for identifying vermiculite sources: *Microscopy and Microanalysis*, v. 10, p. 904–905, doi:10.1017/S1431927604882461.
- Montel, J.-M., Foret, S., Veschambre, M., Nicollet, C., and Provost, A., 1996, Electron microprobe dating of monazite: *Chemical Geology*, v. 131, p. 37–53, doi:10.1016/0009-2541(96)00024-1.
- Mottram, C.M., Warren, C.J., Regis, D., Roberts, N.M.W., Harris, N.B.W., Argles, T.W., and Parrish, R.R., 2014, Developing an inverted Barrovian sequence; insights from monazite petrochronology: *Earth and Planetary Science Letters*, v. 403, p. 418–431, doi:10.1016/j.epsl.2014.07.006.

- Paton, C., Woodhead, J.D., Hellstrom, J.C., Hergt, J.M., Greig, A., and Maas, R., 2010, Improved laser ablation U-Pb zircon geochronology through robust downhole fractionation correction: *Geochemistry, Geophysics, Geosystems*, v. 11, doi:10.1029/2009GC002618.
- Schmitz M.D. and Bowring S.A., 2001. U-Pb zircon and titanite systematics of the Fish Canyon Tuff: an assessment of high-precision U-Pb geochronology and its application to young volcanic rocks. *Geochimica et Cosmochimica Acta*, v. 65(15), p.2571-2587. [https://doi.org/10.1016/S0016-7037\(01\)00616-0](https://doi.org/10.1016/S0016-7037(01)00616-0)
- Schoene, B., Crowley, J.L., Condon, D.J., Schmitz, M.D., and Bowring, S.A., 2006, Reassessing the uranium decay constants for geochronology using ID-TIMS U–Pb data: *Geochimica et Cosmochimica Acta*, v. 70, p. 426–445, doi:10.1016/j.gca.2005.09.007.
- Sláma J., Košler J., Condon D.J., Crowley J.L., Gerdes A., Hancher J.M., Horstwood M.S.A., Morris G.A., Nasdala L., Norberg N., Schaltegger U., Schoene B., Tubrett M.N., Whitehouse M.J., 2008. Plešovice zircon – A new natural reference material for U-Pb and Hf isotopic microanalysis. *Chemical Geology*, v. 249 (1-2), p. 1 – 35. <https://doi.org/10.1016/j.chemgeo.2007.11.005>
- Stern, R., and Rayner, N., 2003, Ages of several xenotime megacrysts by ID-TIMS: potential reference materials for ion microprobe U–Pb geochronology: *Radiogenic Age and Isotopic Studies: Report 16. Geological Survey of Canada, Current Research 2003-F1*, p. 7.
- Swayze, G.A., Lowers, H.A., Benzel, W.M., Clark, R.N., Driscoll, R.L., Perlman, Z.S., Hoefen, T.M., and Dyar, M.D., 2018, Characterizing the source of potentially asbestos-bearing commercial vermiculite insulation using in situ IR spectroscopy: *American Mineralogist*, v. 103, p. 517–549, doi:10.2138/am-2018-6022.
- Vermeesch, P., 2018, IsoplotR: A free and open toolbox for geochronology: *Geoscience Frontiers*, v. 9, p. 1479–1493, doi:10.1016/j.gsf.2018.04.001.
- White, R.W., Powell, R., and Holland, T.J.B., 2007, Progress relating to calculation of partial melting equilibria for metapelites: *Journal of Metamorphic Geology*, v. 25, p. 511–527, doi:10.1111/j.1525-1314.2007.00711.x.
- White, R.W., Powell, R., Holland, T.J.B., Johnson, T.E., and Green, E.C.R., 2014, New mineral activity–composition relations for thermodynamic calculations in metapelitic systems: *Journal of Metamorphic Geology*, v. 32, p. 261–286, doi:10.1111/jmg.12071.
- White, Powell, Holland, and Worley, 2000, The effect of TiO₂ and Fe₂O₃ on metapelitic assemblages at greenschist and amphibolite facies conditions: mineral equilibria calculations in the system K₂O–FeO–MgO–Al₂O₃–SiO₂–H₂O–TiO₂–Fe₂O₃: *Journal of Metamorphic Geology*, v. 18, p. 497–511, doi:10.1046/j.1525-1314.2000.00269.x.
- Whitney, D.L., and Evans, B.W., 2010, Abbreviations for names of rock-forming minerals: *American Mineralogist*, v. 95, p. 185–187, doi:10.2138/am.2010.3371.

- Wiedenbeck, M. et al., 2004, Further Characterisation of the 91500 Zircon Crystal: *Geostandards and Geoanalytical Research*, v. 28, p. 9–39, doi:10.1111/j.1751-908X.2004.tb01041.x.
- Williams, M.L., Jercinovic, M.J., Goncalves, P., and Mahan, K., 2006, Format and philosophy for collecting, compiling, and reporting microprobe monazite ages: *Chemical Geology*, v. 225, p. 1–15, doi:10.1016/j.chemgeo.2005.07.024.
- Williams, M.L., Jercinovic, M.J., and Hetherington, C.J., 2007, Microprobe monazite geochronology: Understanding geologic processes by integrating composition and chronology: *Annual Review of Earth and Planetary Sciences*, v. 35, p. 137–175, doi:10.1146/annurev.earth.35.031306.140228.
- Williams, M.L., Jercinovic, M.J., Mahan, K.H., and Dumond, G., 2017, Electron microprobe petrochronology: *Reviews in Mineralogy and Geochemistry*, v. 83, p. 153–182, doi:10.2138/rmg.2017.83.5.
- Xiang, H., and Connolly, J.A.D., 2022, GeoPS: An interactive visual computing tool for thermodynamic modelling of phase equilibria: *Journal of Metamorphic Geology*, v. 40, p. 243–255, doi:10.1111/jmg.12626.



Figure. S1: Outcrop and hand sample photos of sample locality 21IWH05. (A-B) Images of outcrop near Vallecito Campground. (C) Close-up image of outcrop. (D) Collected hand sample.



Figure S2: Images of sample 21WH07 collected on Potato Hill, near Coal Bank Pass in the western Needle Mountains. (A) Sampled garnet-bearing outcrop. Outcrop forms ~2 m long, low ledge. (B-C) Close up images of sampled outcrop, hand lens for scale. Note that sampling avoided late, leucocratic veins. (D) Additional image of sampled outcrop. (E) Image of collected hand sample with garnet.

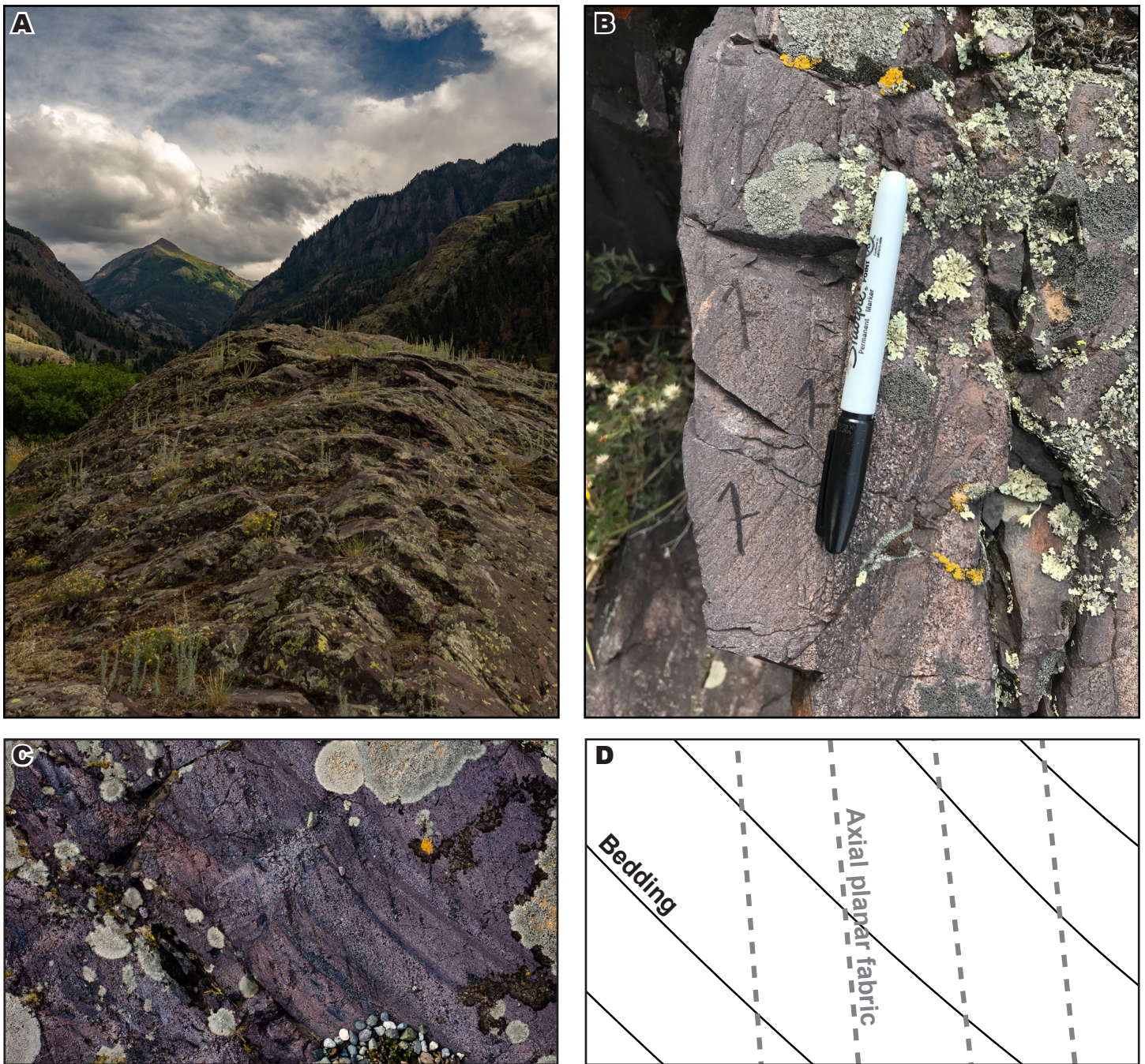


Figure. S3: Images of Uncompahgre Formation sample 21IWH11. (A) Sample locality within the Uncompahgre Gorge, south of Ouray. Rock is pink, medium- to coarse-grained, meta-quartz arenite. (B) Close up of sampled outcrop. Note Primary bedding and axial planar cleavage. (C) Close up of sampled outcrop highlighting bedding and axial planar fabrics. (D) Sketch of outcrop shown in Figure S3C highlighting the fabric relationships.



Figure S4: Drill core sample 21IWH18. (A) Photograph of drill core; note dark biotite-rich gneiss matrix with granitic pegmatite (pink, center-right and upper left) and folded quartz-rich vein (center). (B) Close up of sampled drill core interval. Biotite-rich gneiss with K-feldspar (pink). (C) Close up of sharp contact between biotite-rich paragneiss and cross-cutting granitic pegmatite.



Figure S5: (A-B) Granite of Cataract Gulch, sample locality 21AG06. (C) Sample locality for sample 21IWH04 of Bakers Bridge Granite. (D) Close up image of coarse-grained Bakers Bridge Granite.



Figure S6: (A, B) Twilight Gneiss exposed at Electra Lake. Lighter portion of outcrop sampled for U-Pb zircon geochronology (21IWH03). (C) Eolus Granite float at Vallecito Campground. (D) Hornblende-biotite Eolus Granite float hand sample (21IWH06) collected for U-Pb zircon geochronology.

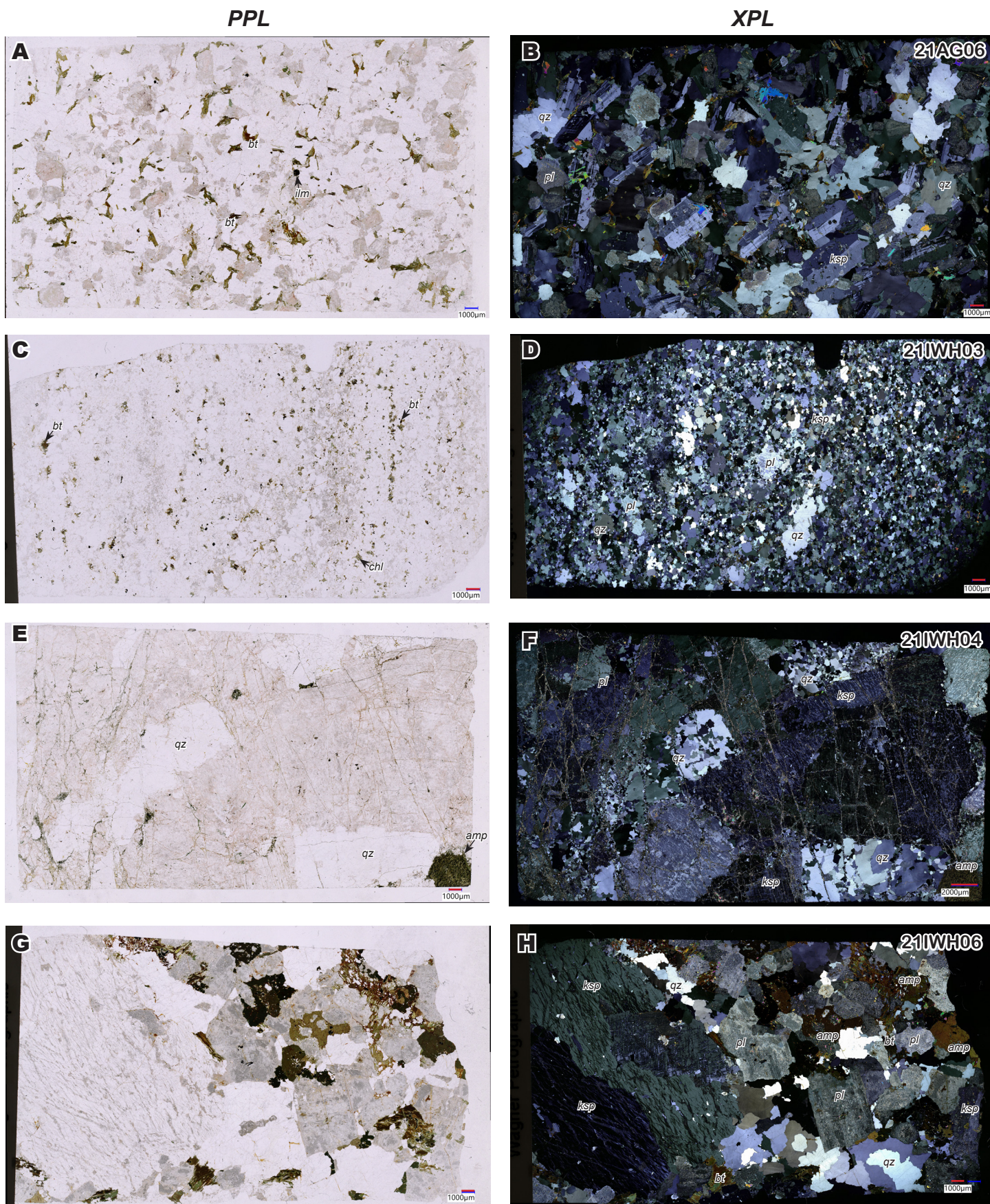


Figure S7: Plane (PPL) and cross polarized (XPL) scans of entire polished thin sections of igneous rocks analyzed for U-Pb zircon geochronology by LA-ICP-MS. PPL images to left and XPL images to right. Granite of Cataract Gulch sample 21AG06 (A, B); Twilight Gneiss sample 21IWH03B (C, D); Bakers Bridge Granite sample 21IWH04 (E, F), Eolus Granite sample 21IWH06 (G, H).

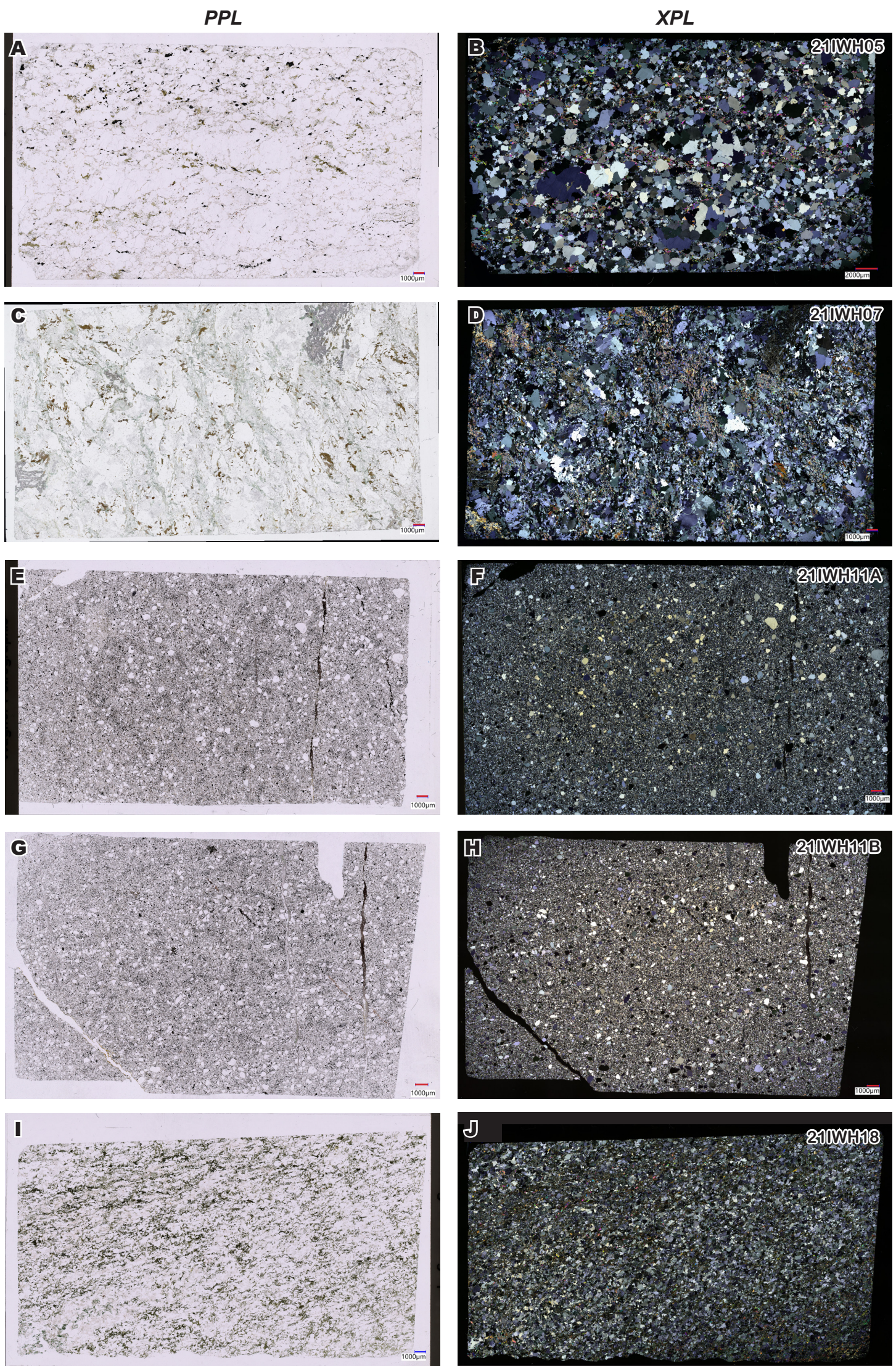


Figure S8: Plane (PPL) and cross polarized (XPL) scans of entire polished thin sections from metamorphic rocks analyzed for monazite and/or xenotime geochronology. Plane polarized (PPL) images to left and cross polarized (XPL) images to right. Samples: 21IWH05 (A, B), 21IWH07 (C, D), 21IWH11A (E, F), 21IWH11B (G, H), and 21IWH18 (I, J).

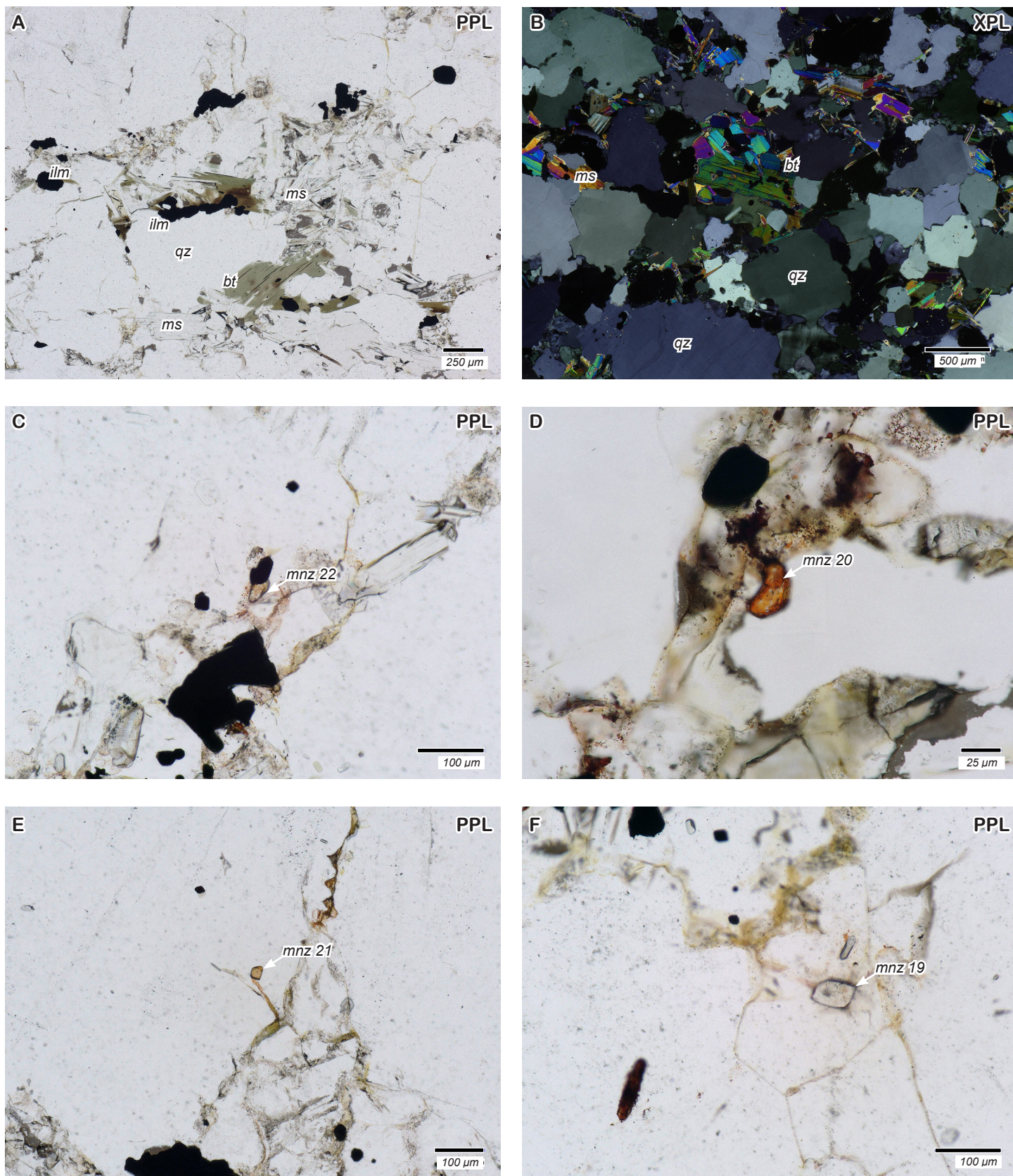


Figure S9: Photomicrographs from sample 21IWH05. (A) Interpreted peak assemblage including quartz, muscovite, biotite, and ilmenite (opaque) in plane polarized light (PPL). (B) Interpreted peak assemblage including quartz, muscovite, biotite, and ilmenite (opaque) in cross polarized light (XPL). (C-F) Photomicrographs showing microstructural context of dated monazite grains mnz22 (C), mnz20 (D), mnz21 (E), and mnz19 (F).

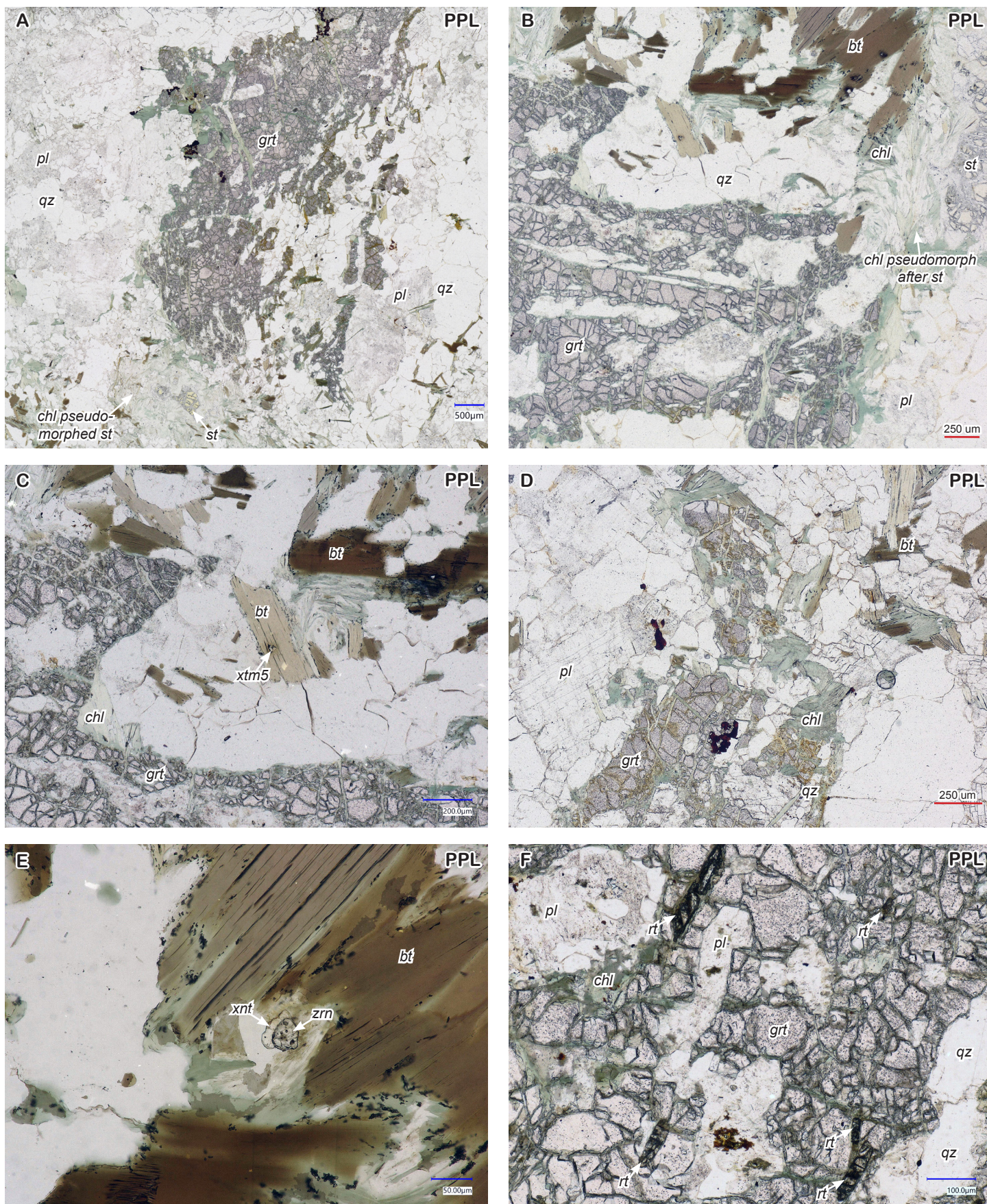


Figure S10: Photomicrographs of sample 21IWH07. (A) PPL showing garnet, plagioclase, staurolite (largely pseudomorphed to chlorite), and quartz. (B) Garnet and largely pseudomorphed staurolite. (C) Xenotime in retrograde zone near garnet. (D) Rutile inclusions in garnet parallel to S1 fabric. (D) Xenotime on zircon near resorbed garnet. (E) Garnet overgrown by (now pseudomorphed) staurolite.

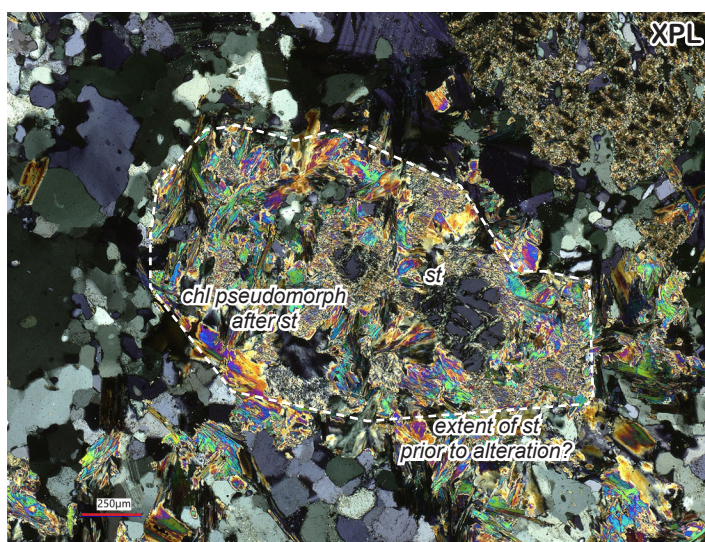
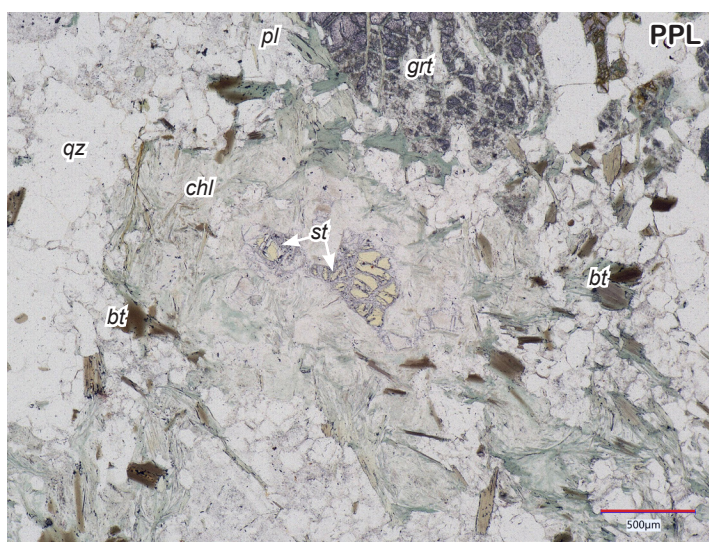
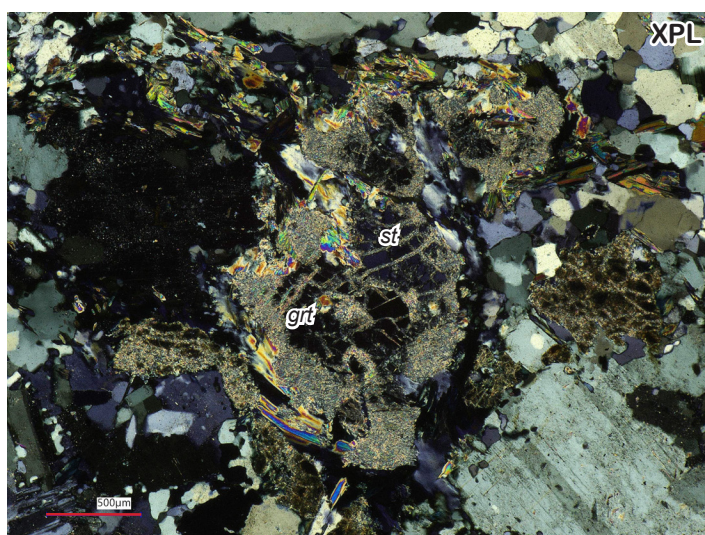
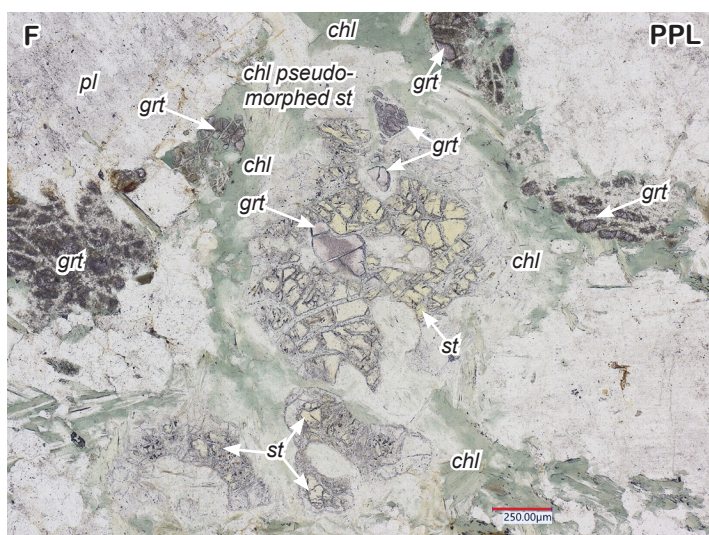
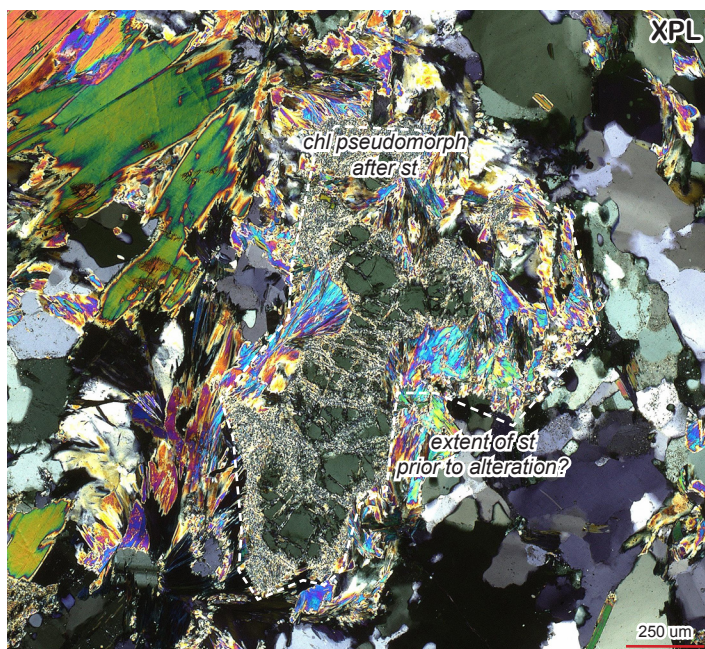


Figure S10 continued: Plane (PPL) and cross (XPL_ polarized photomicrographs of staurolite in sample 21IWH07. Images are labeled with phases and apparent extent of staurolite prior to retrogression, as indicated by chlorite pseudomorphs, are outlined.

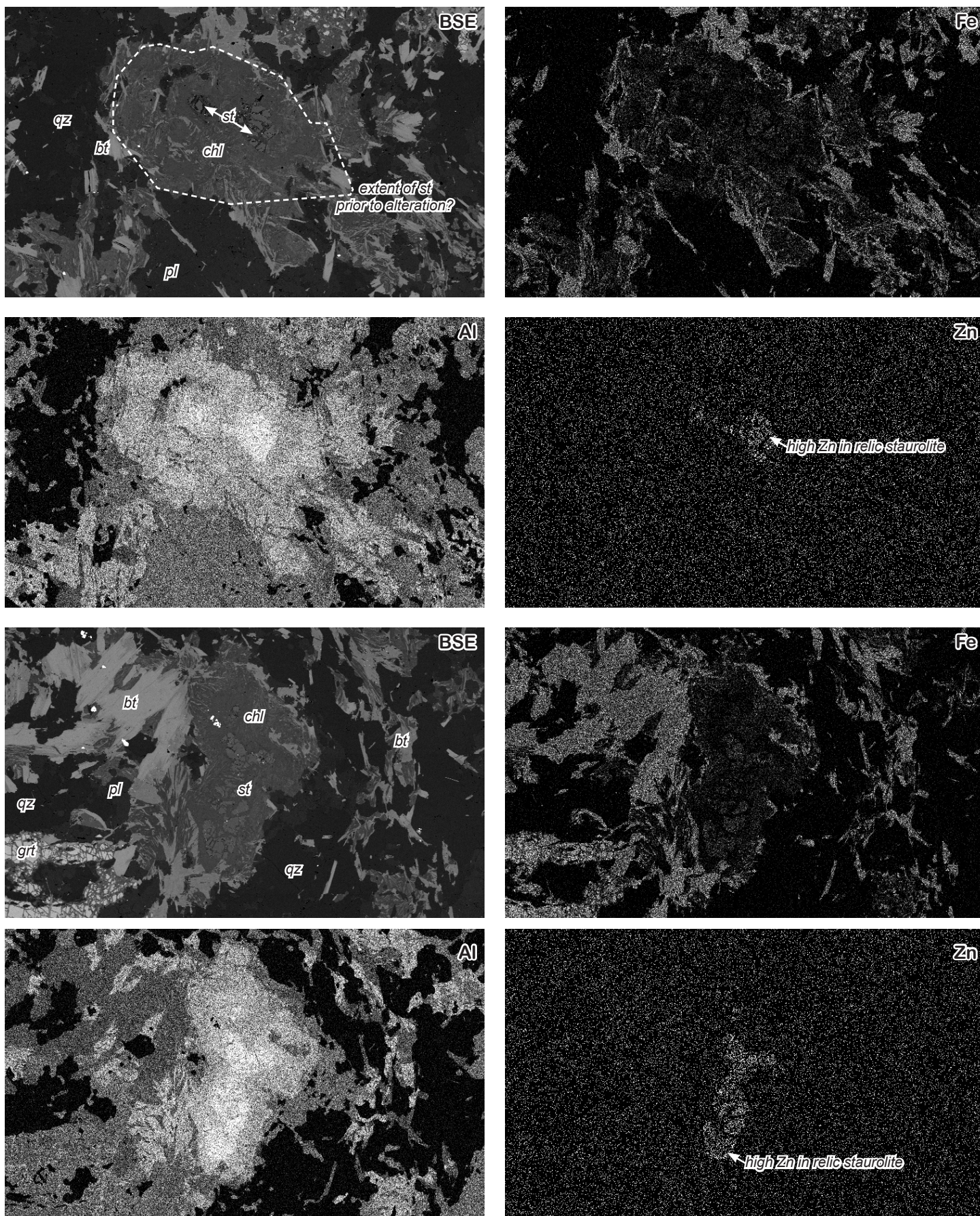
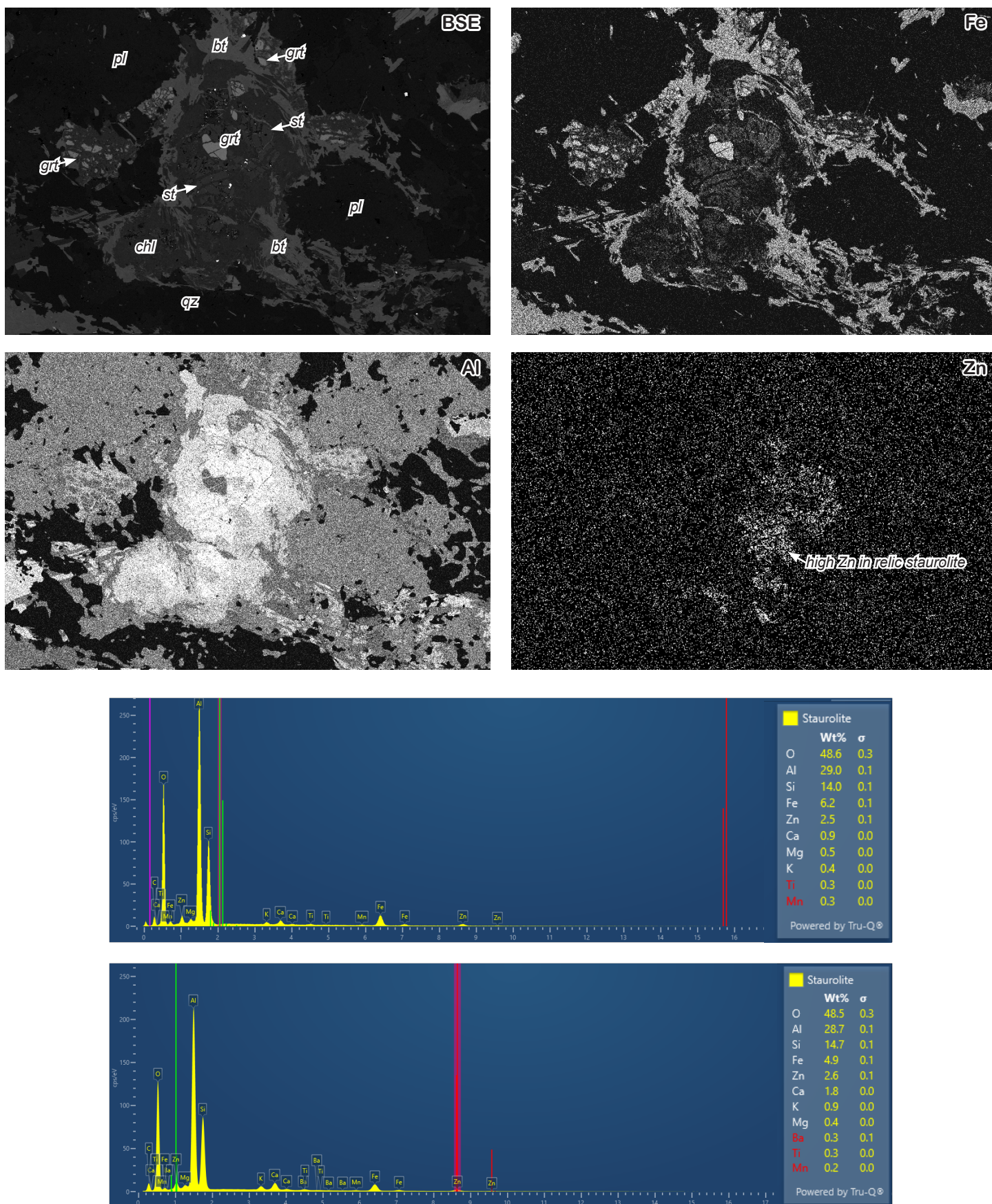


Figure S10 continued: Scanning electron microscope (SEM) backscattered electron (BSE) images and Fe, Al, and Zn EDS compositional maps of staurolite grains from sample 21IWH07.



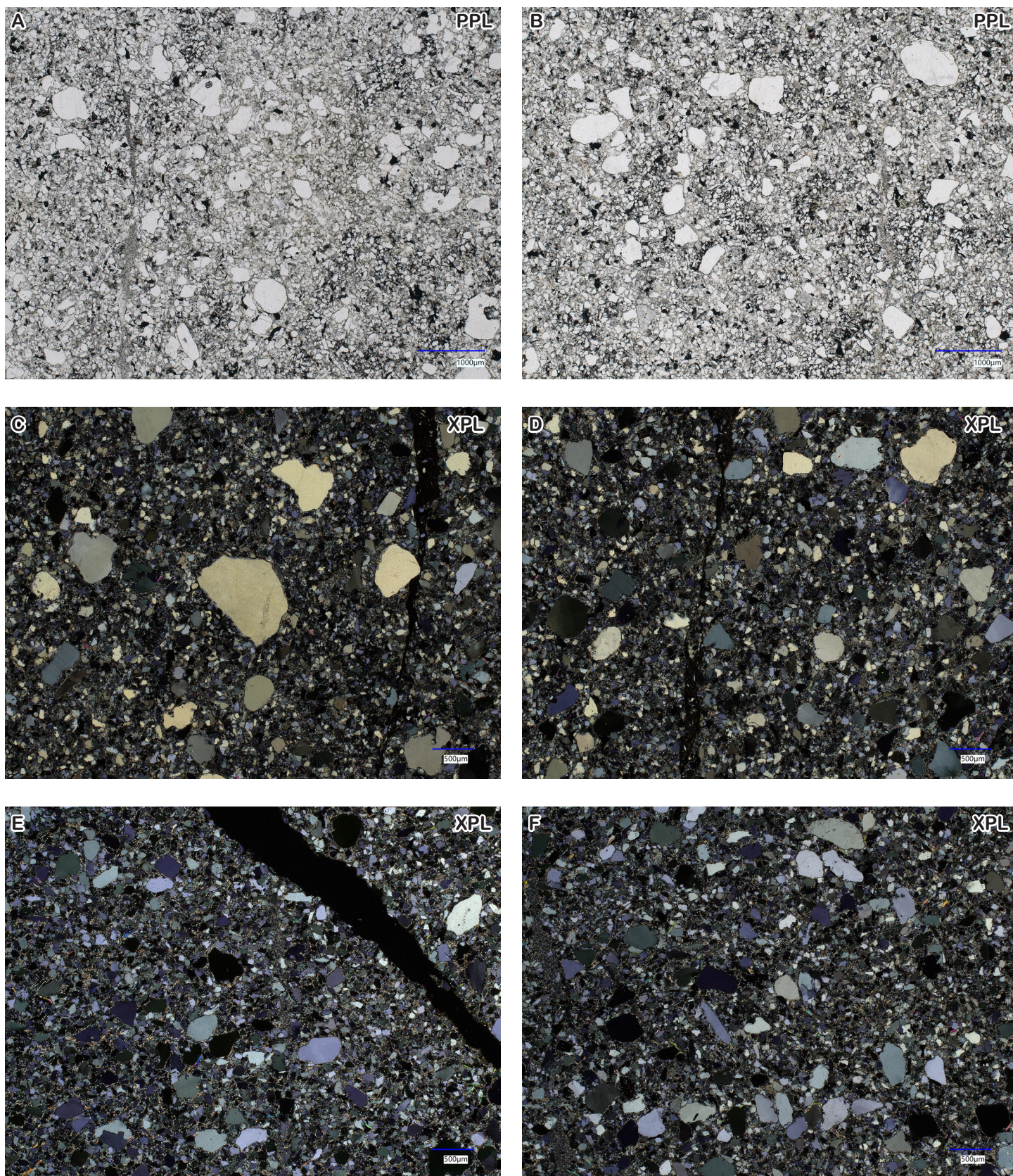


Figure S11: Photomicrographs of sample 21WH11. (A) and (B) are shown in PPL and (C-F) are XPL. Images show sub-angular to sub-rounded quartz grains in finer grained quartz matrix.

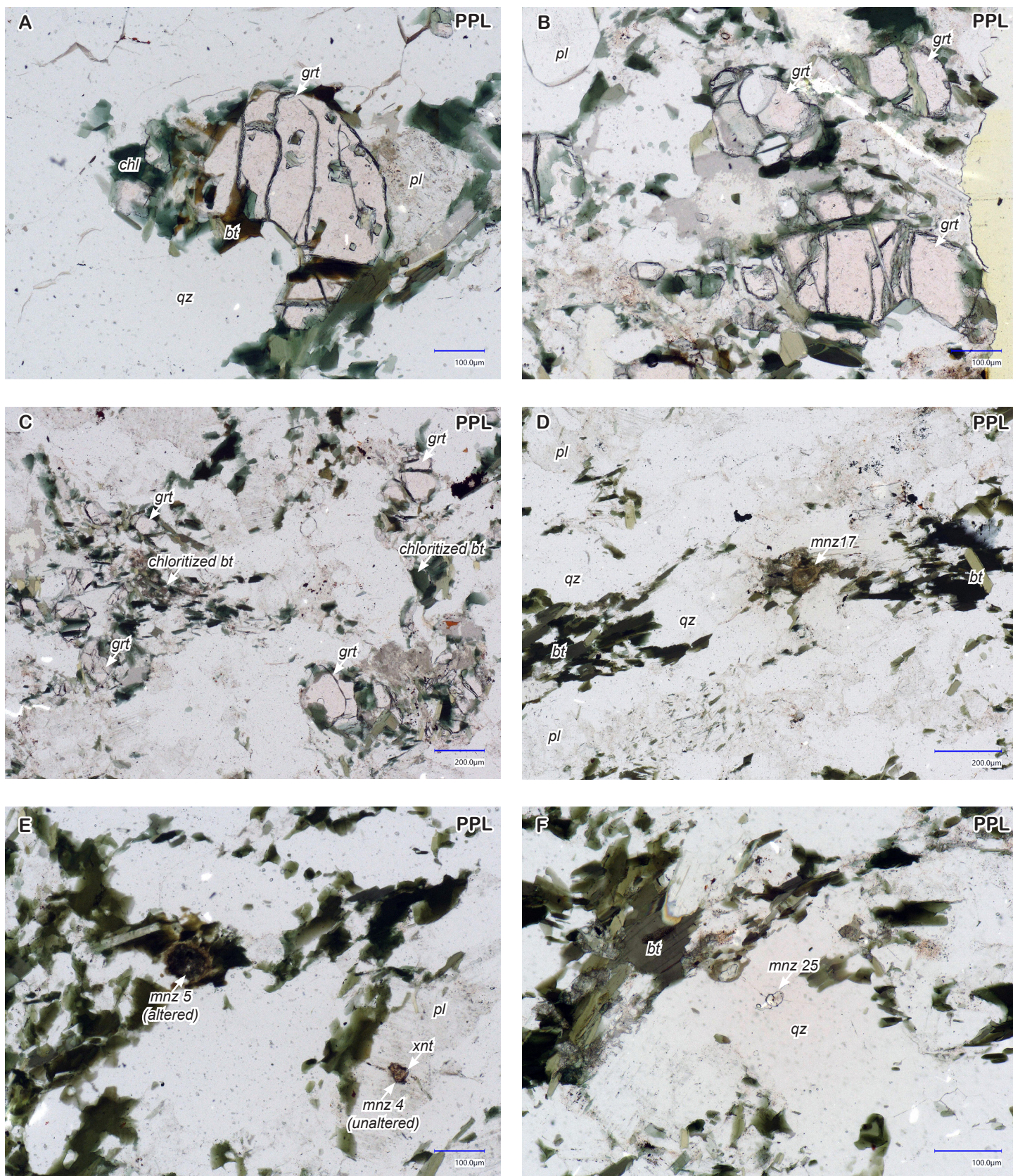


Figure S12: Selected photomicrographs of drill core sample 21IWH18. (A-C) Garnet locally rimmed by retrograde biotite (retrograded in places to chlorite). (D) Altered monazite grain in matrix and in contact with chloritized biotite. (E) Altered monazite grain (mnz 5) within chloritized biotite and matrix and unaltered monazite (mnz 4) in physical contact with unaltered xenotime included within plagioclase. (F) Unaltered monazite grain (mnz 25) included within quartz.

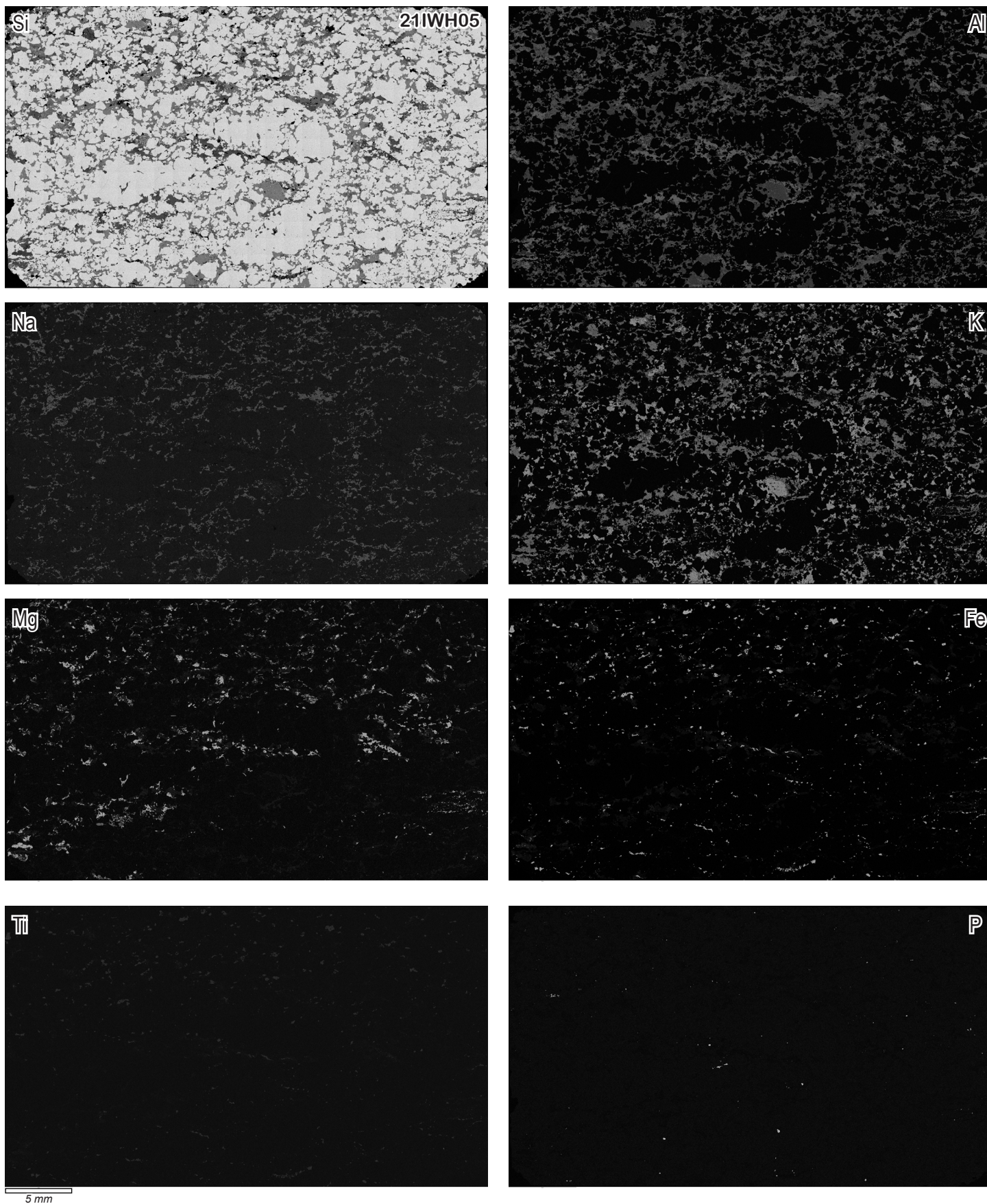


Figure S13: Full thin section EDS compositional maps for sample 21IWH05 labeled by element.

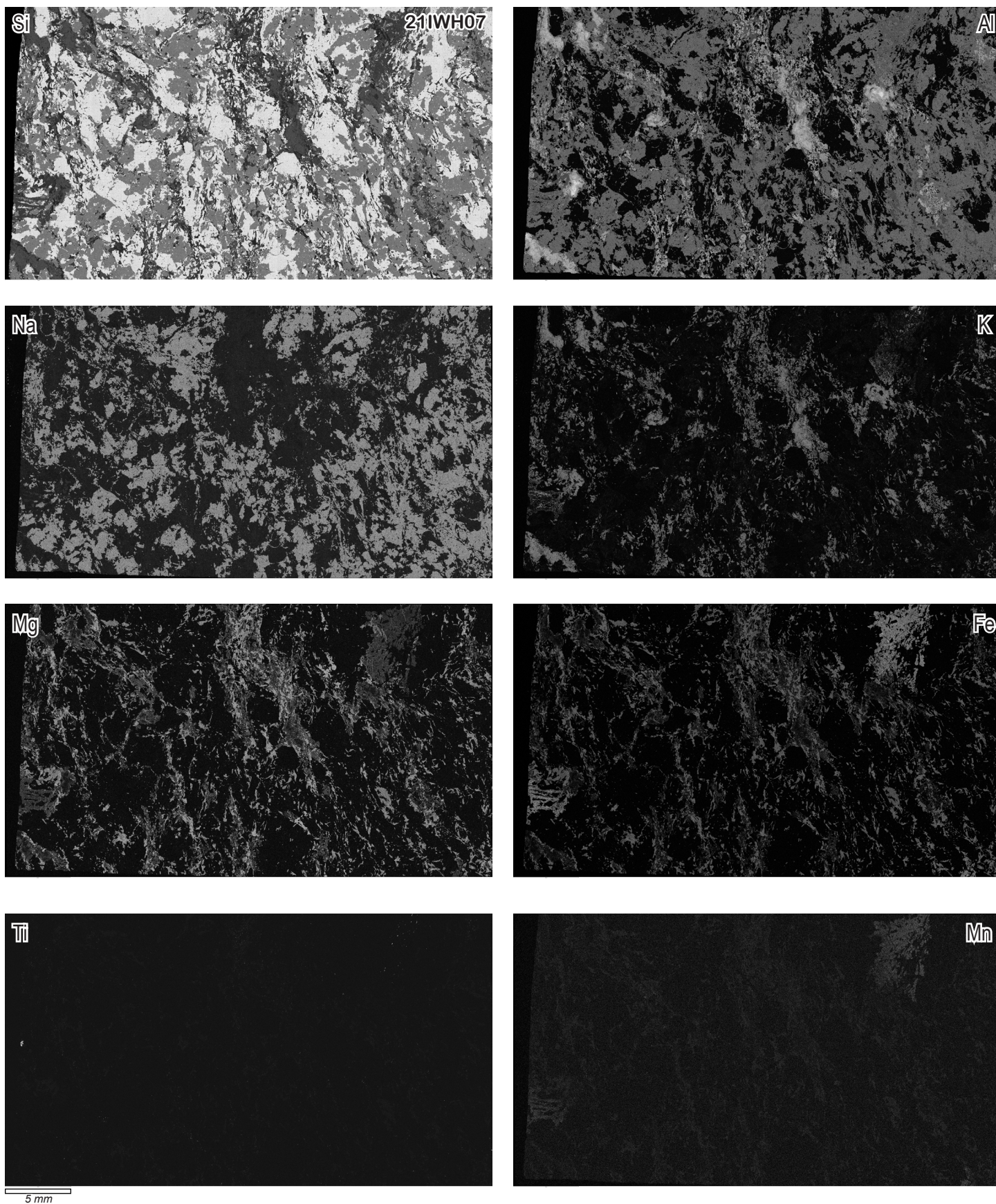


Figure S14: Full thin section EDS compositional maps for sample 21IWH07 labeled by element.

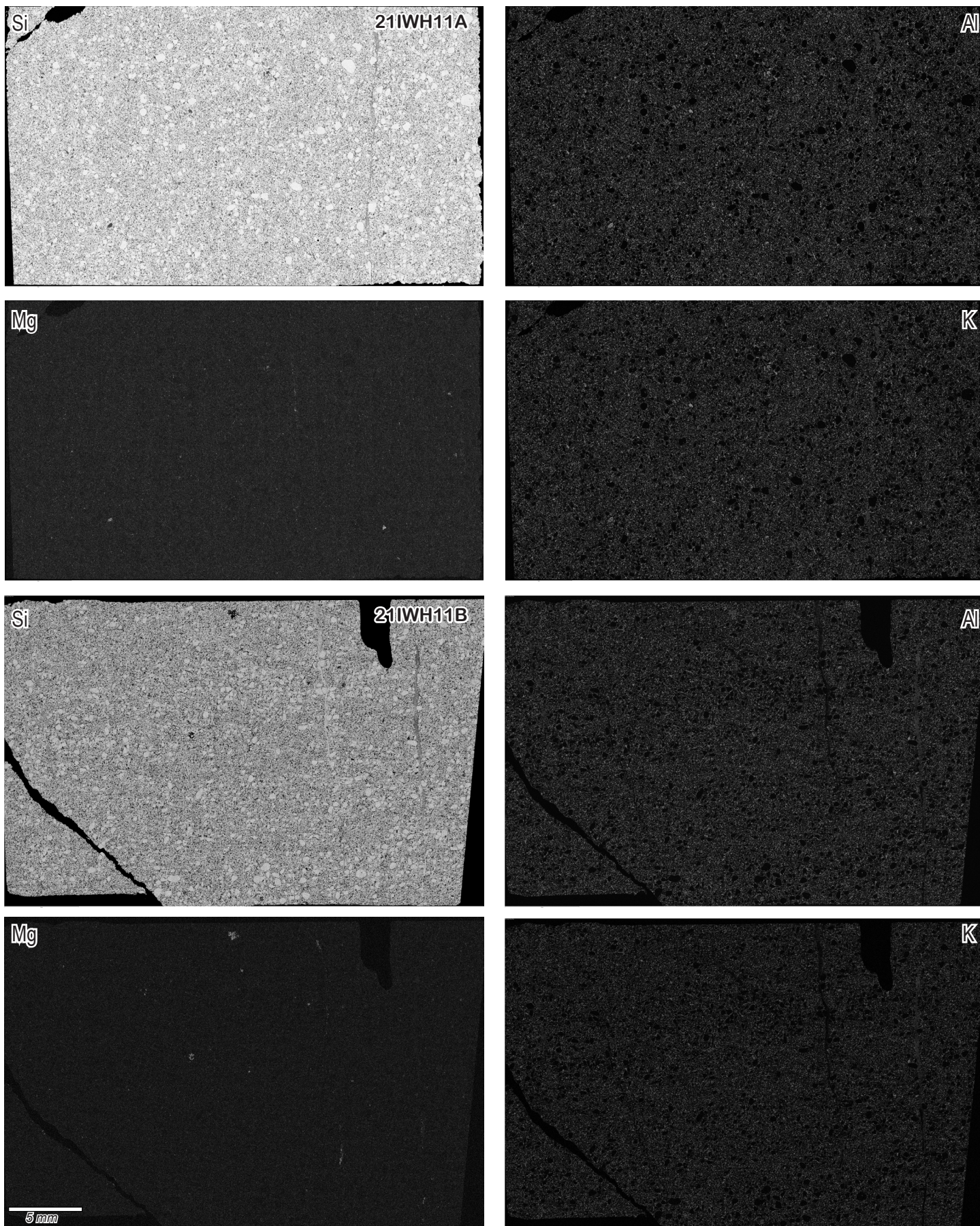


Figure S15: Full thin section EDS compositional maps for samples 21IWH11A (top) and 21IWH11B (bottom). Maps labeled by element and sample.

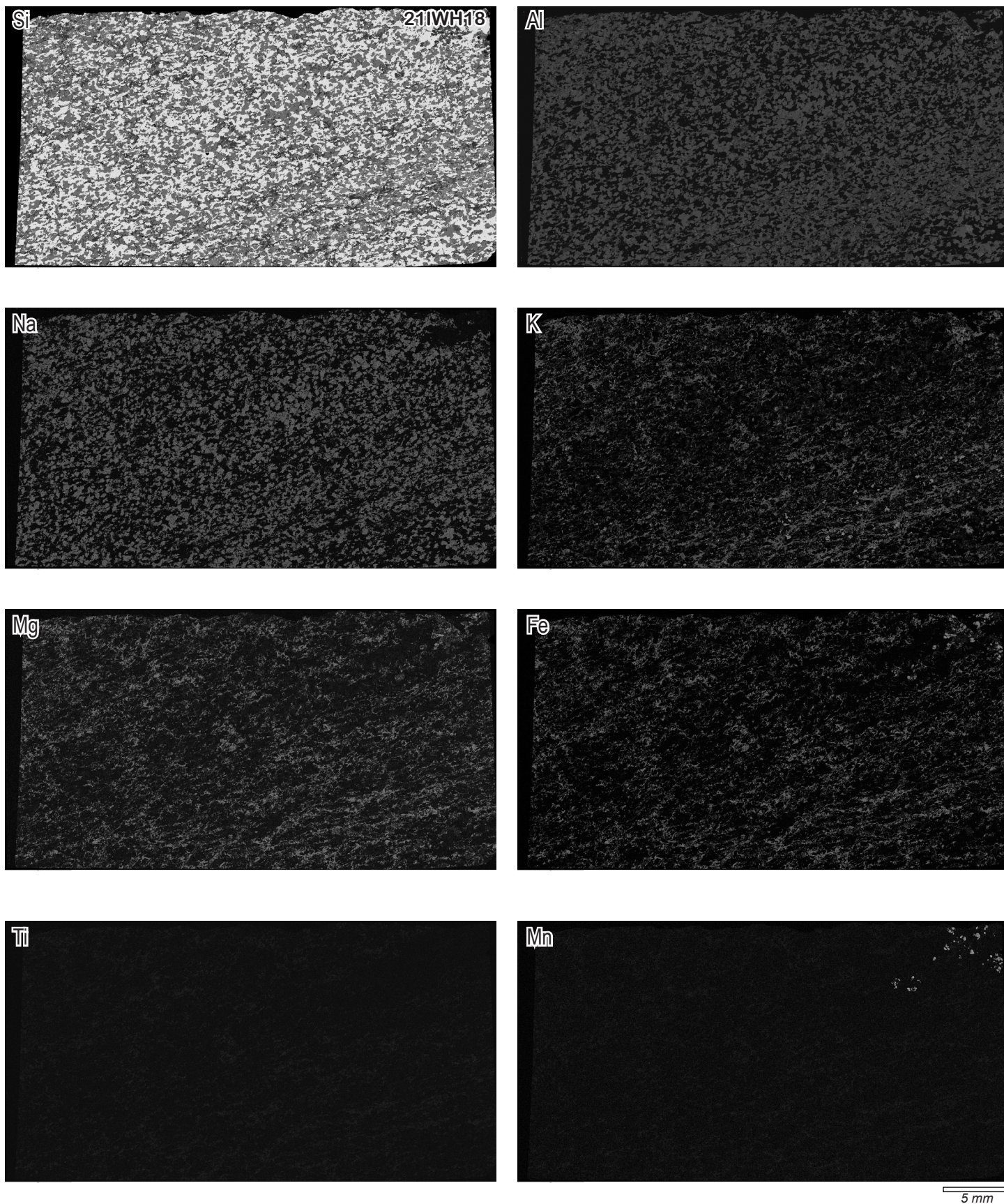


Figure S16: Full thin section EDS compositional maps for sample 21IWH18 labeled by element.

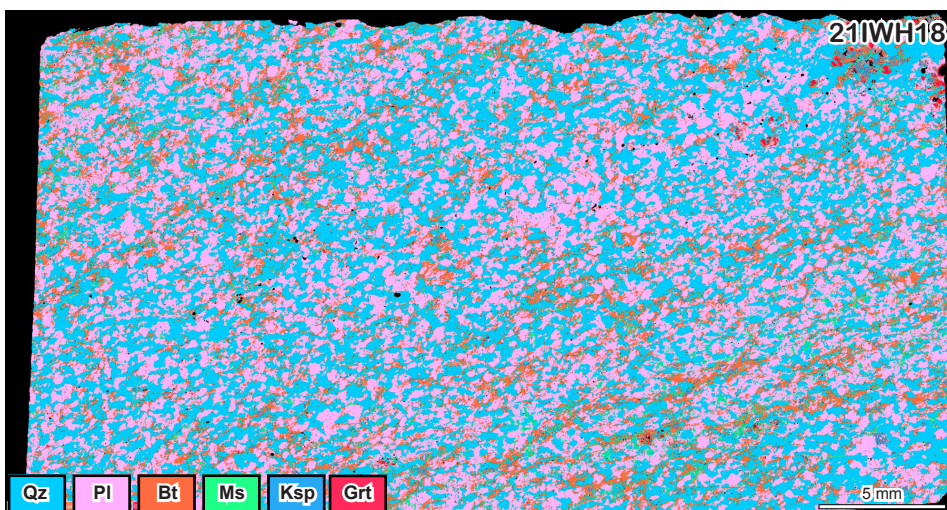
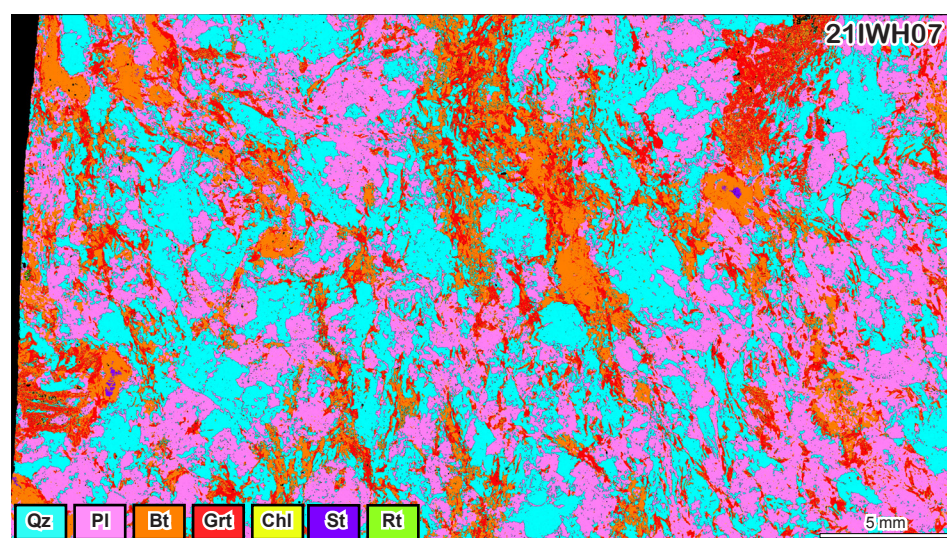
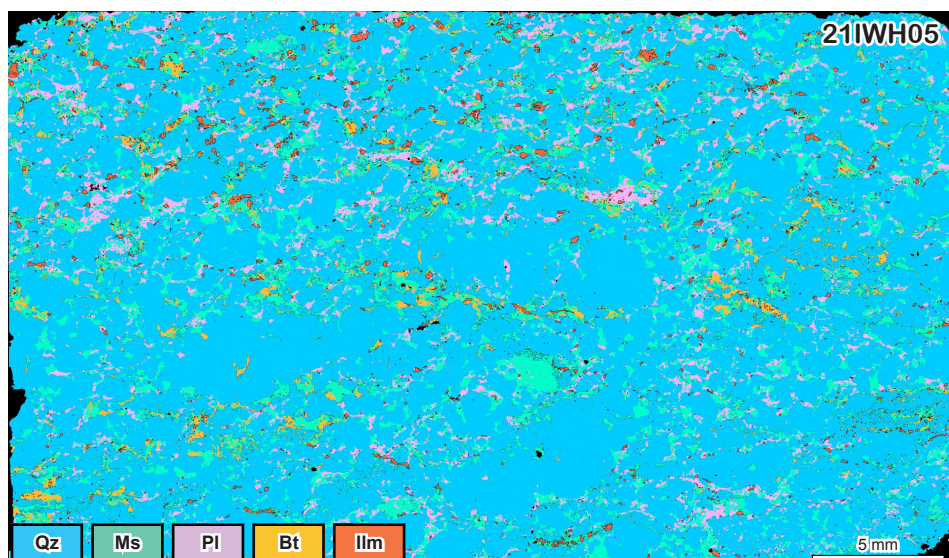


Fig. S17: Full thin section EDS automated major phase maps for samples 21IWH05, 21IWH07, 21IWH11A, and 21IWH18 generated in Aztec 6.0. Color schemes indicated at lower left of each frame. Note that software had difficulty differentiating between biotite and garnet and between biotite and chlorite in sample 21IWH07 and hence have some overlap.

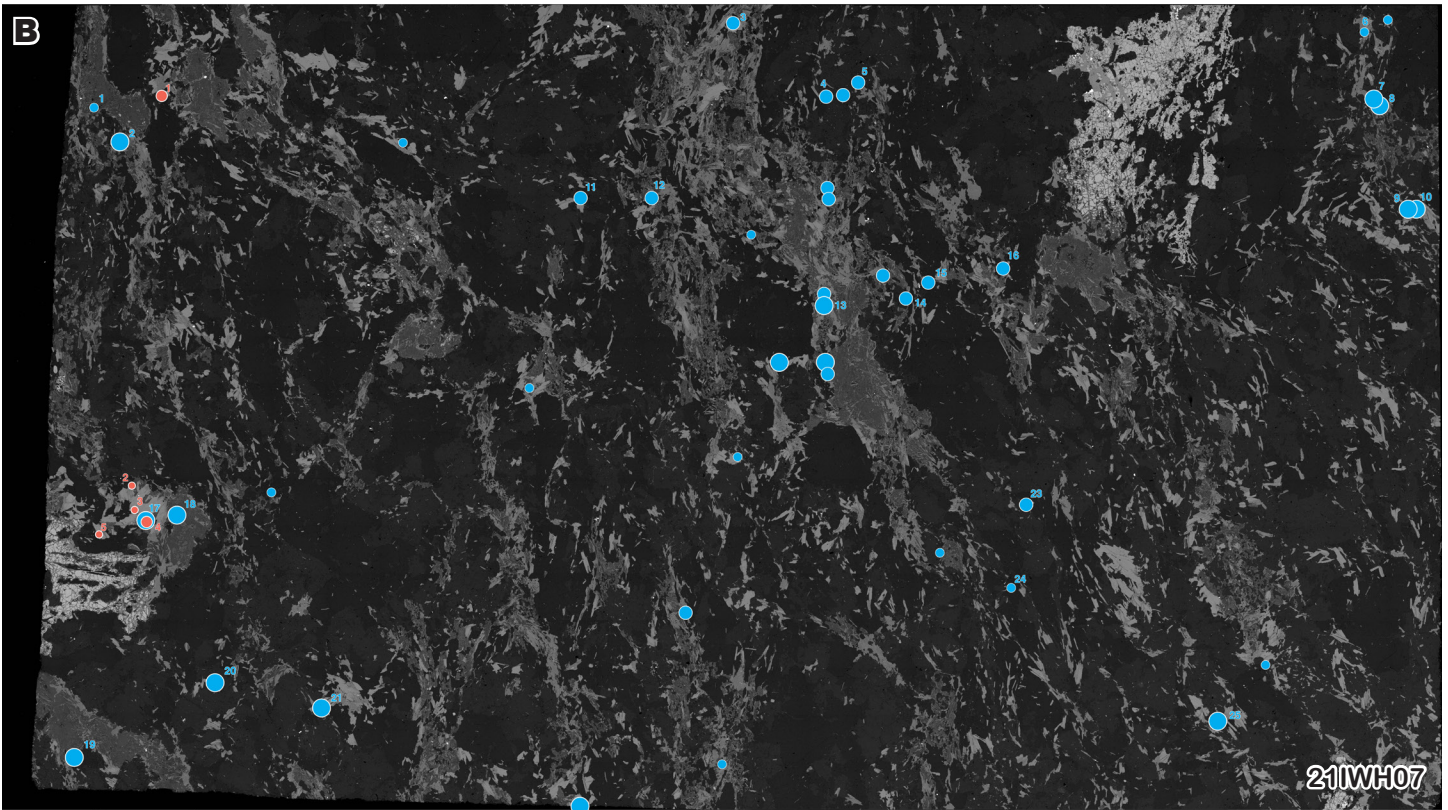
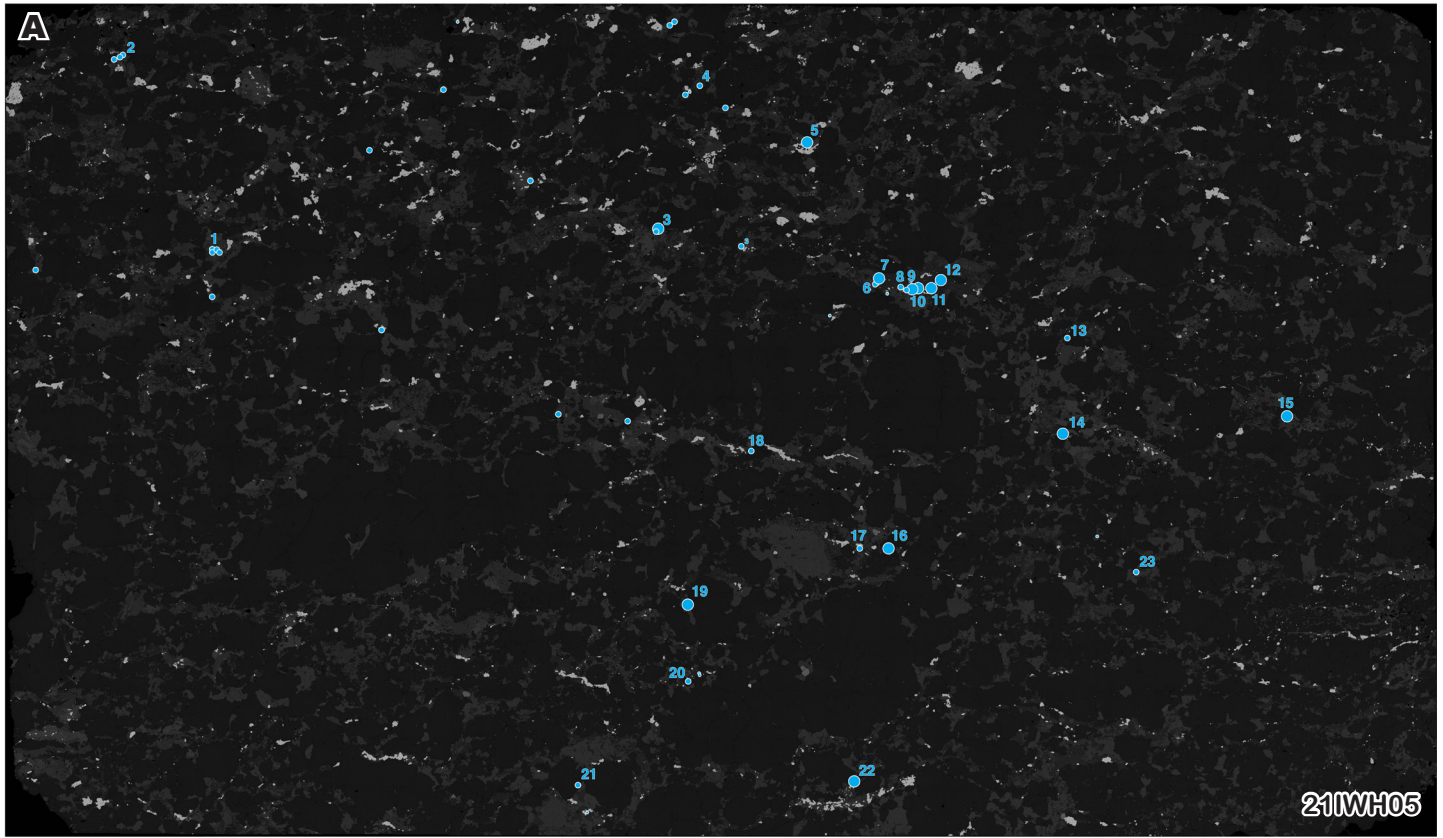


Figure S18: Full thin section backscattered electron (BSE) images overlain with the location of monazite (blue) and xenotime (red) grains. Mapped grains are labeled. (A) 21IWH05. (B) 21IWH07.

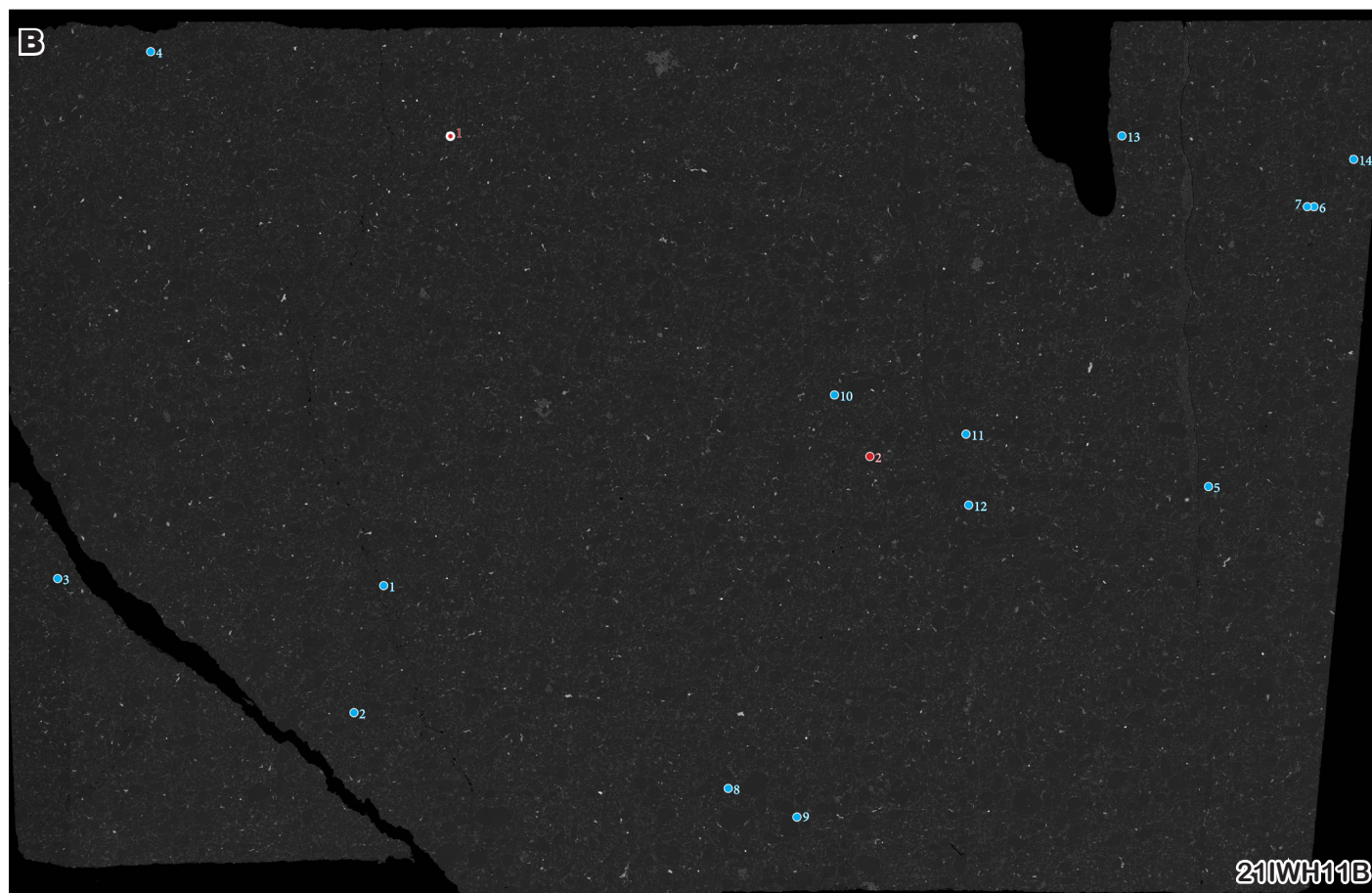
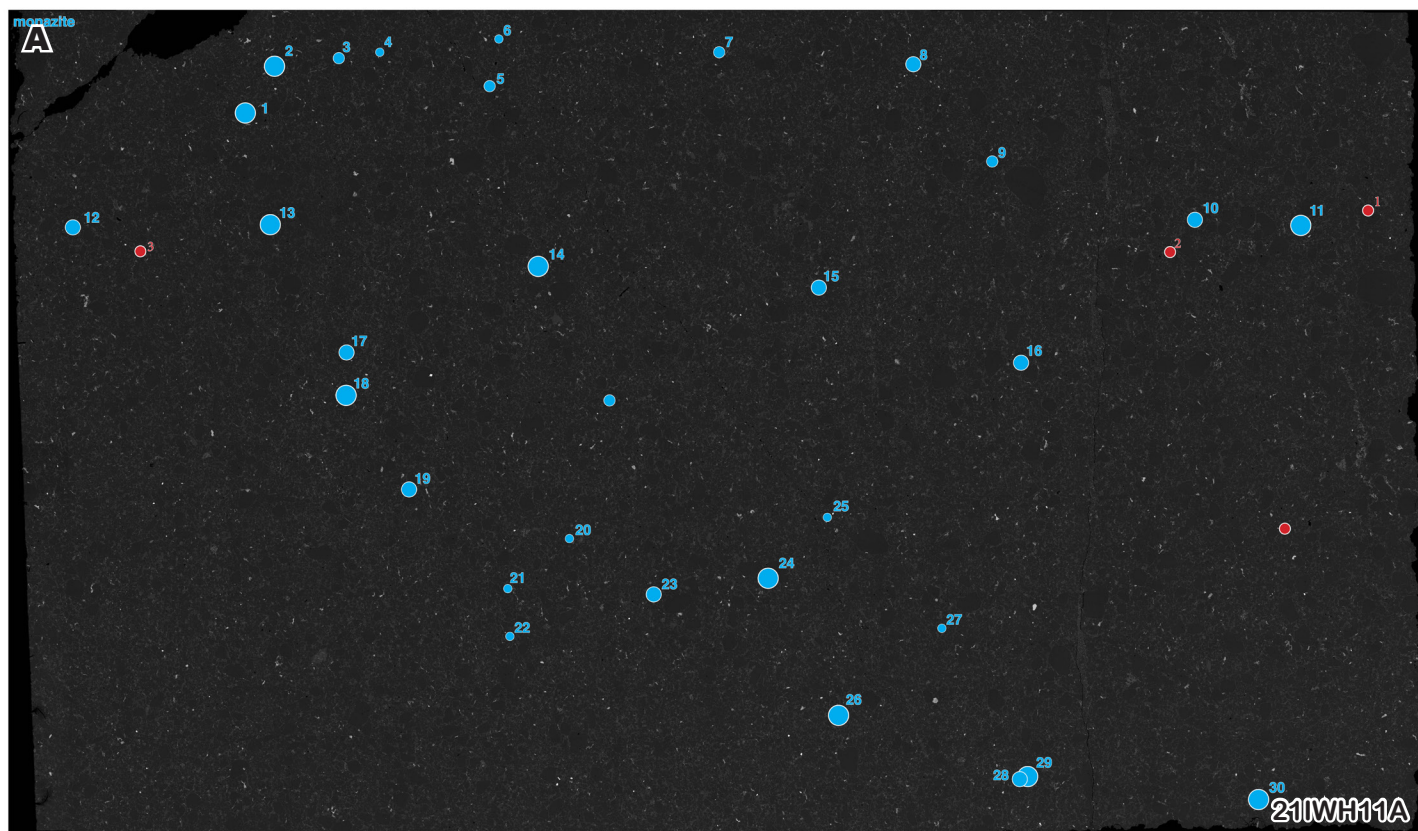


Figure S19: Full thin section backscattered electron (BSE) images overlain with the location of monazite (blue) and xenotime (red) grains. Mapped grains are labeled. (A) 21IWH11A. (B) 21IWH11B.

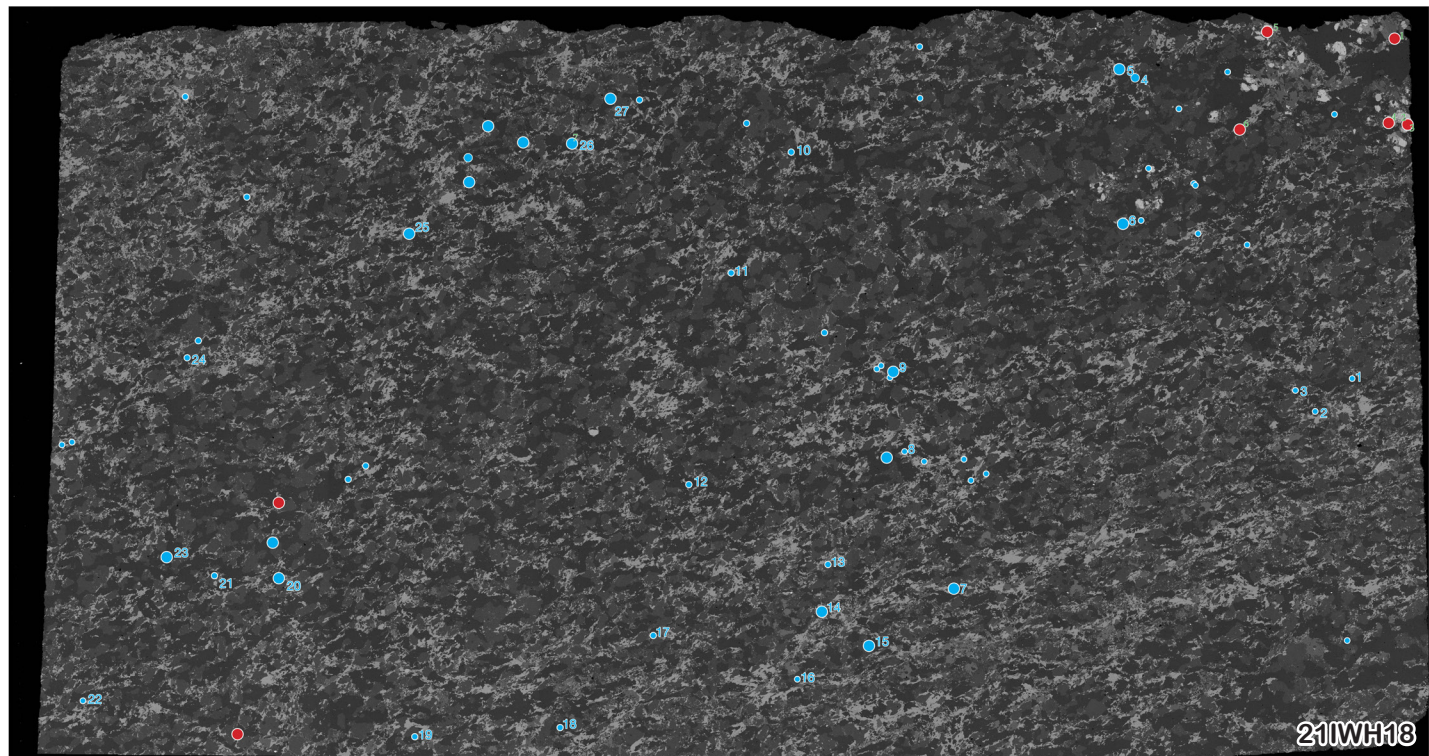


Figure S20: Full thin section backscattered electron (BSE) images overlain with the location of monazite (blue) and xenotime (red) grains for sample 21IWH18. Mapped grains are labeled.

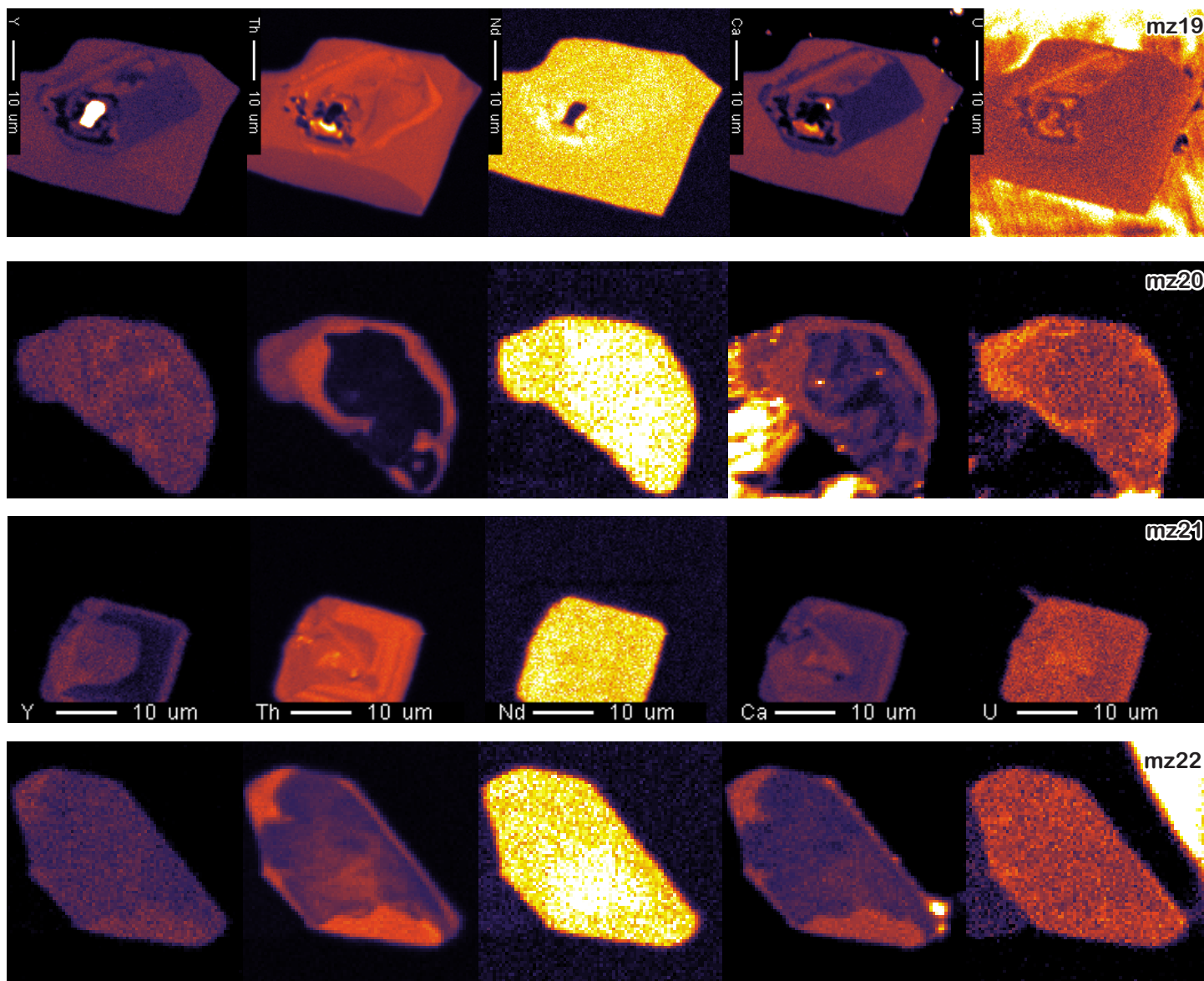


Figure S21A: Simultaneously processed electron microprobe maps (Y, Th, Nd, Ca, U) of dated monazite in sample 21IWH05.

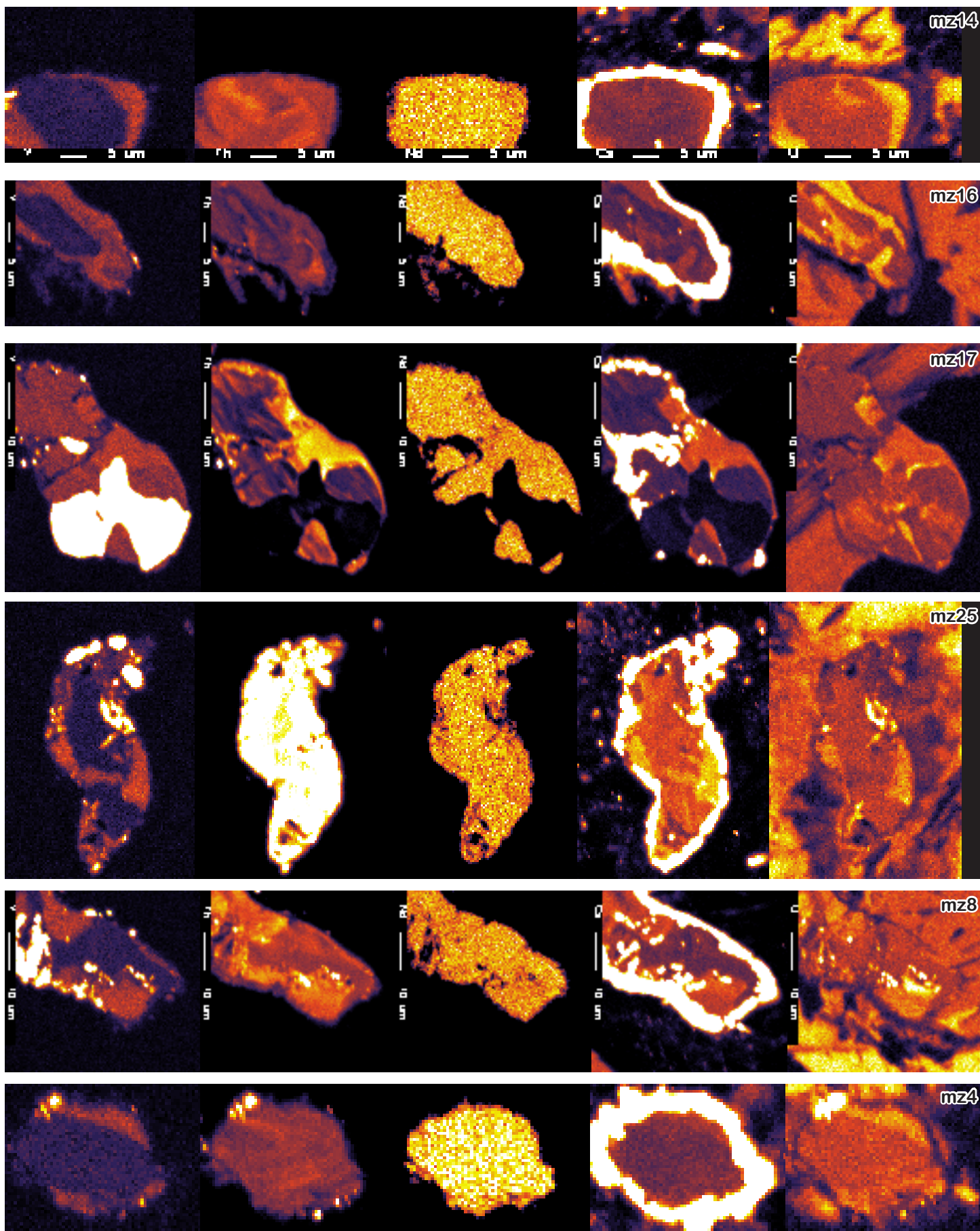


Figure S21B: Simultaneously processed electron microprobe maps (Y, Th, Nd, Ca, U) of dated monazite in sample 21IWH07.

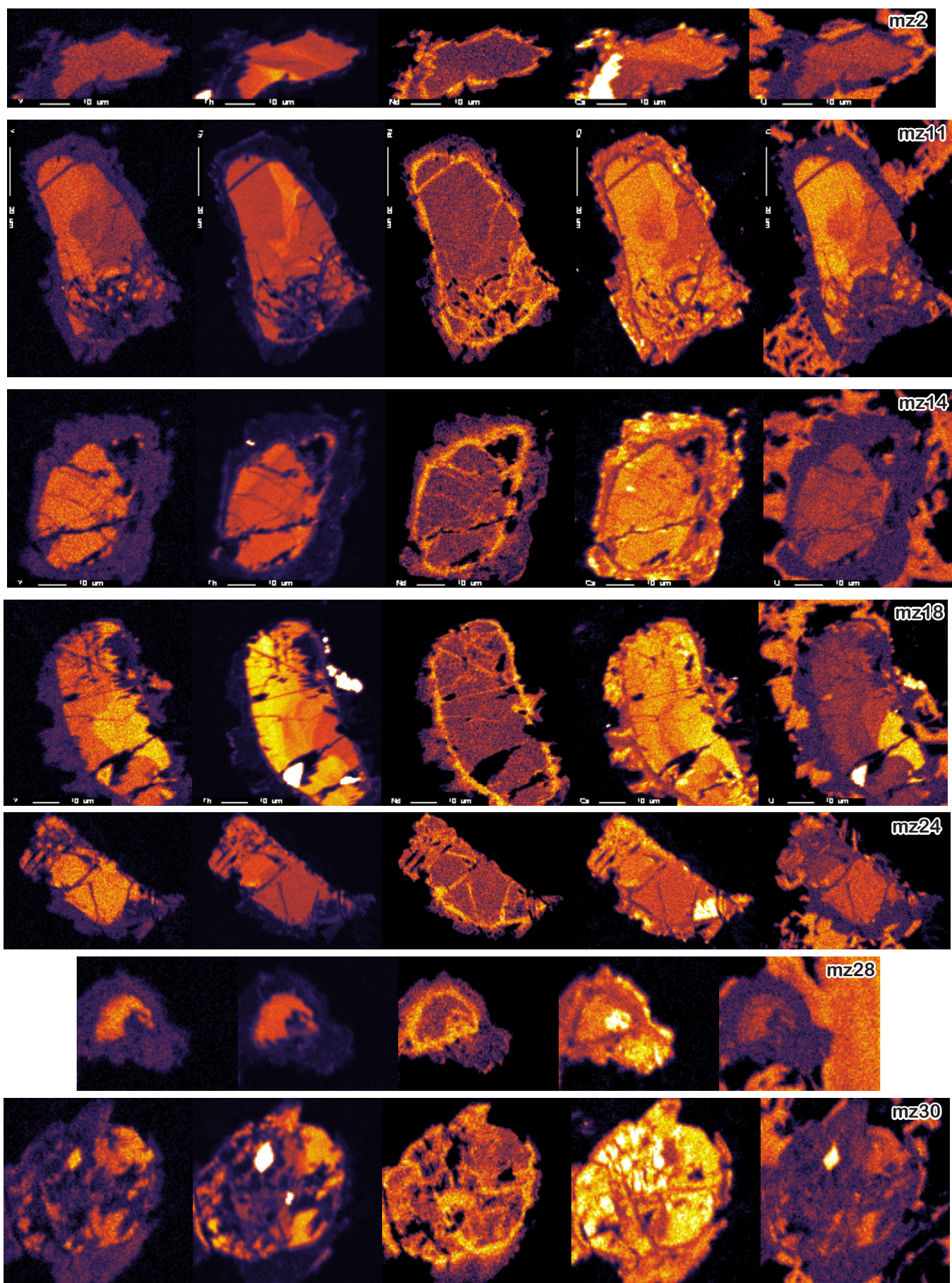


Figure S21C: Simultaneously processed electron microprobe maps (Y, Th, Nd, Ca, U) of analyzed monazite in sample 21IWH11A.

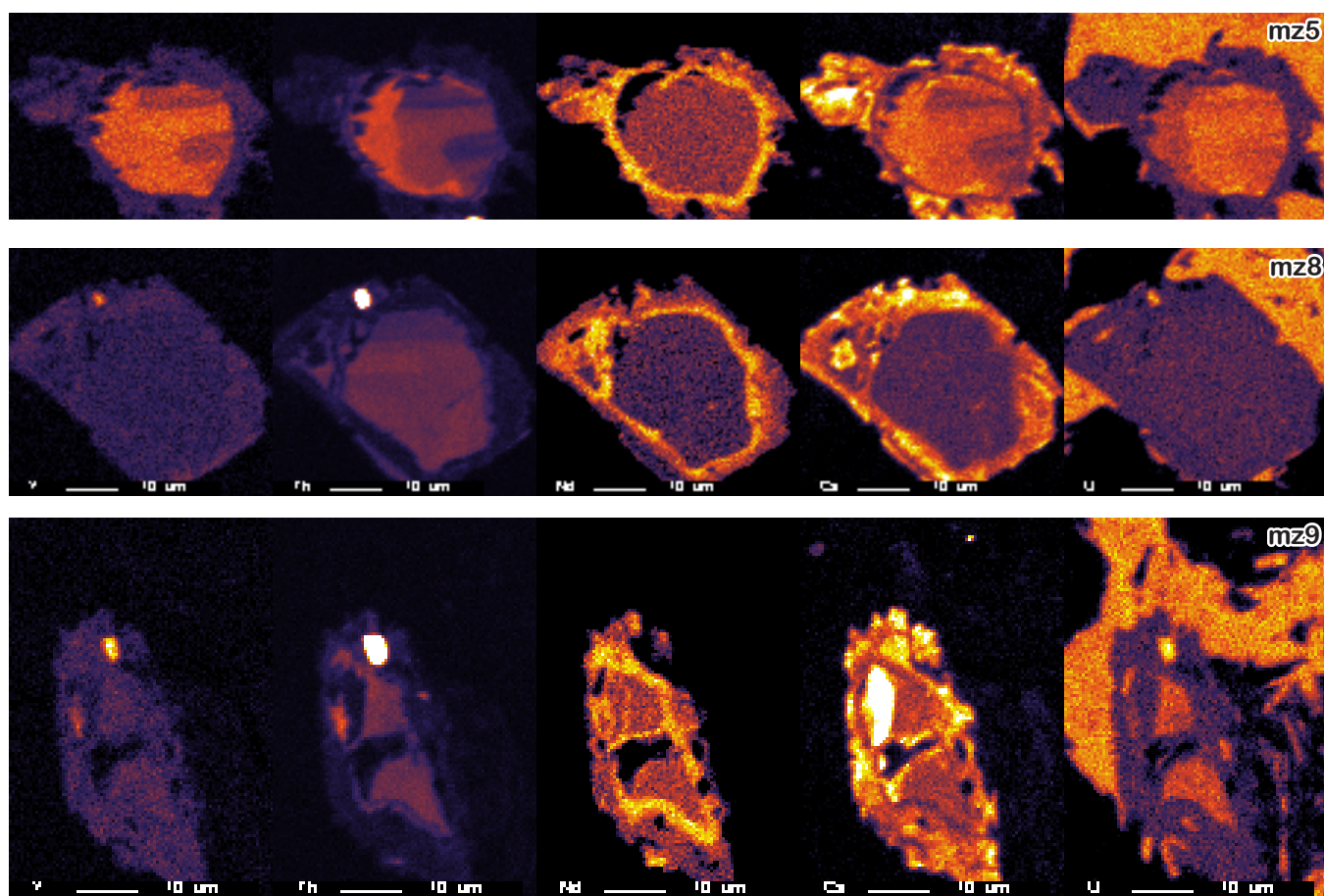


Figure S21D: Simultaneously processed electron microprobe maps (Y, Th, Nd, Ca, U) of analyzed monazite in sample 21IWH11B.

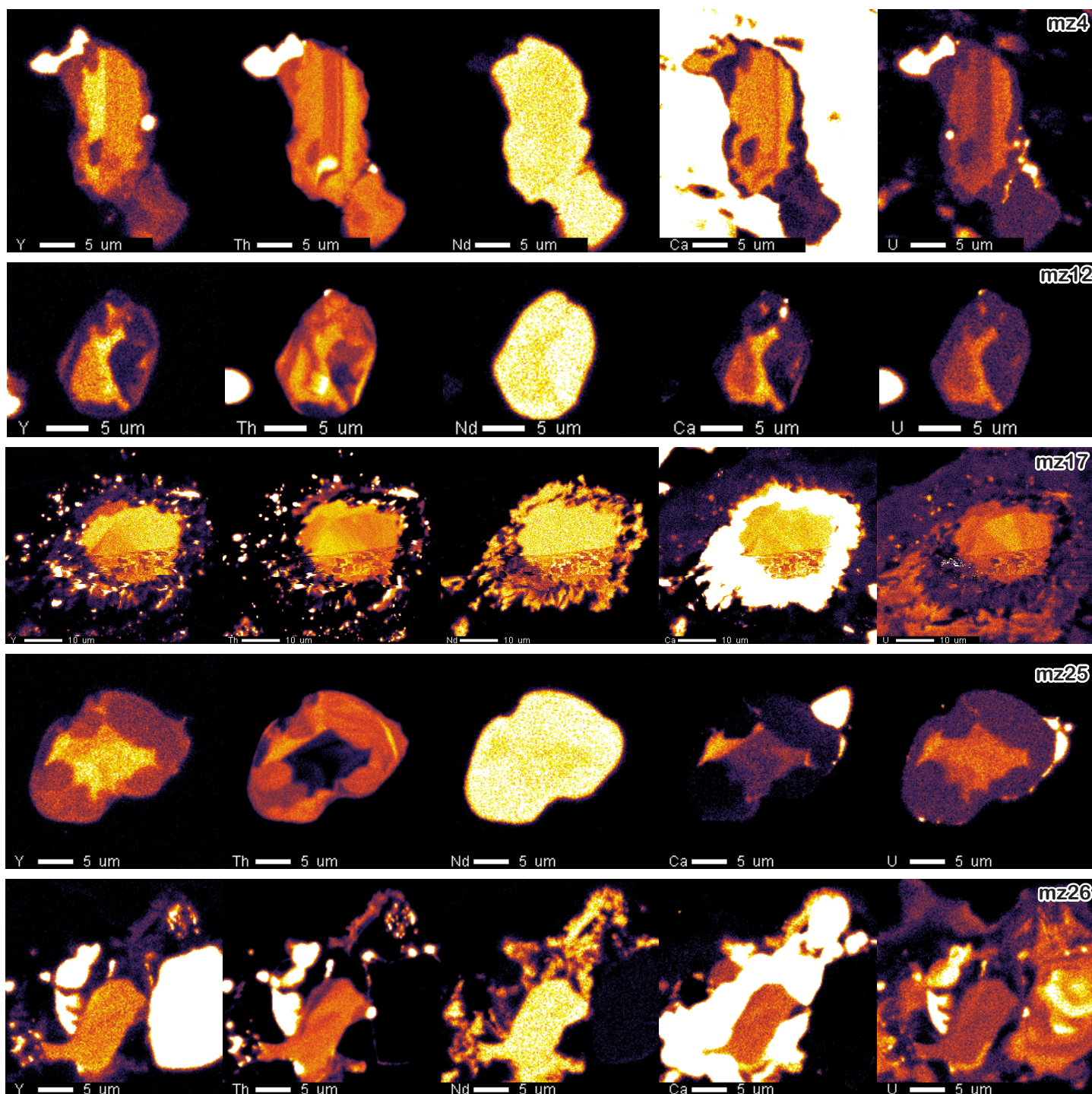


Figure S21E: Simultaneously processed electron microprobe maps (Y, Th, Nd, Ca, U) of dated monazite in sample 21IWH18.

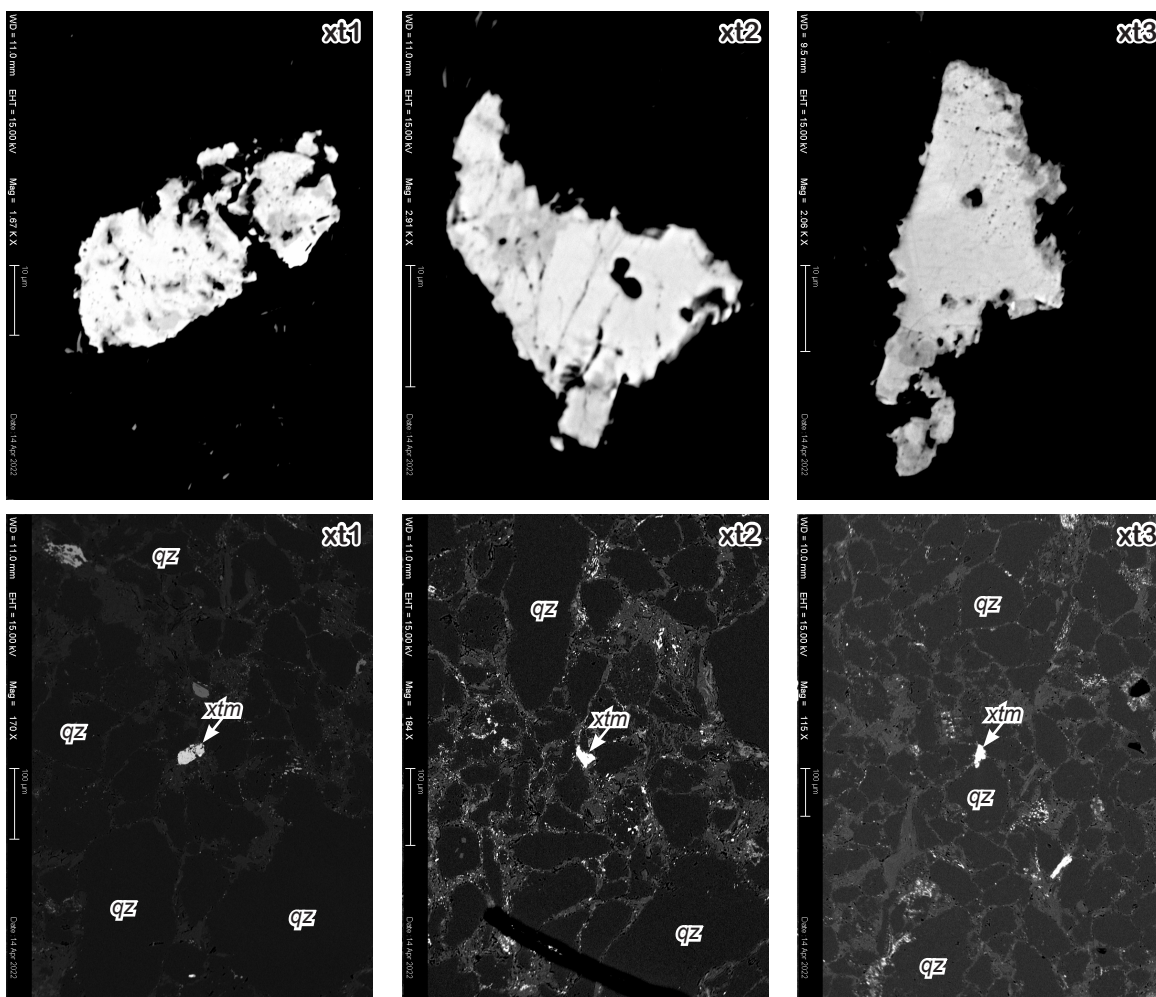


Figure S22A. Backscattered electron (BSE) images of xenotime grains from sample 21IWH11A.

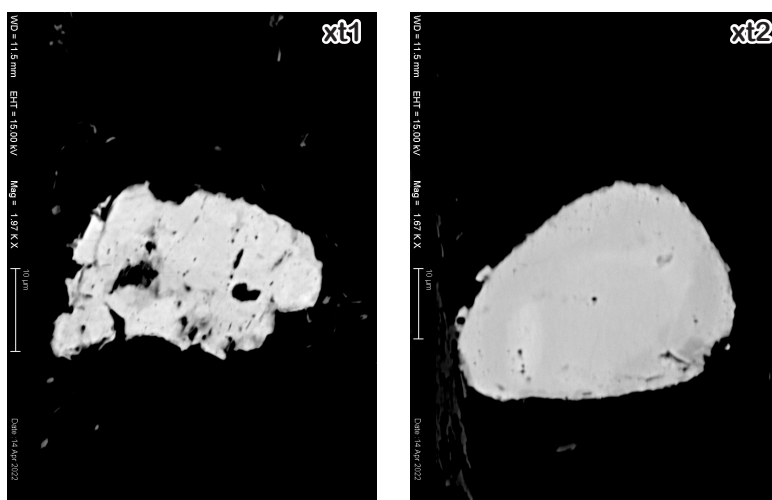


Figure S22B. Backscattered electron (BSE) images of xenotime grains from sample 21IWH11B.

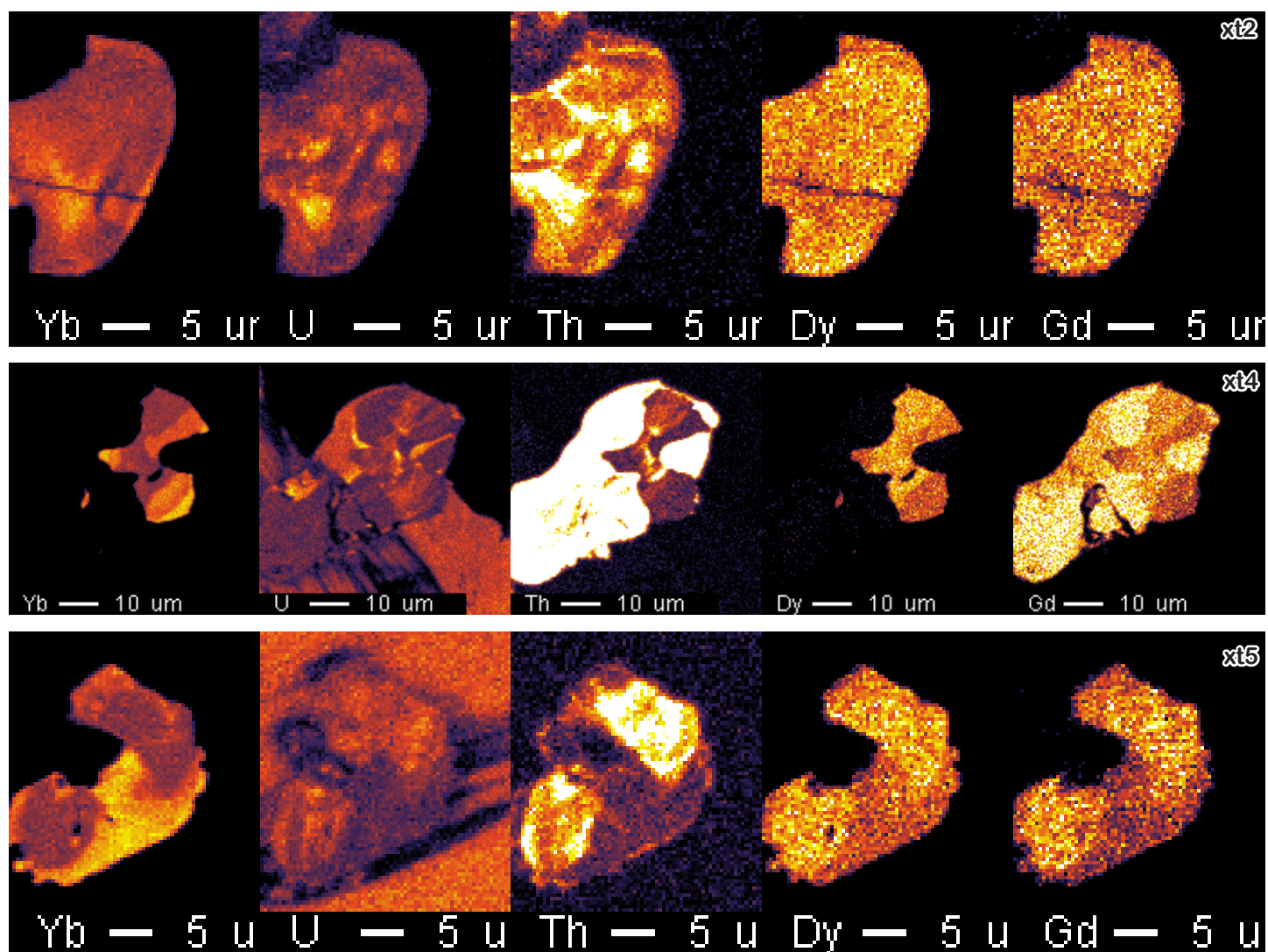


Figure S23A: Simultaneously processed xenotime maps (Yb, U, Th, Dy, Gd) for sample 21IWH07.

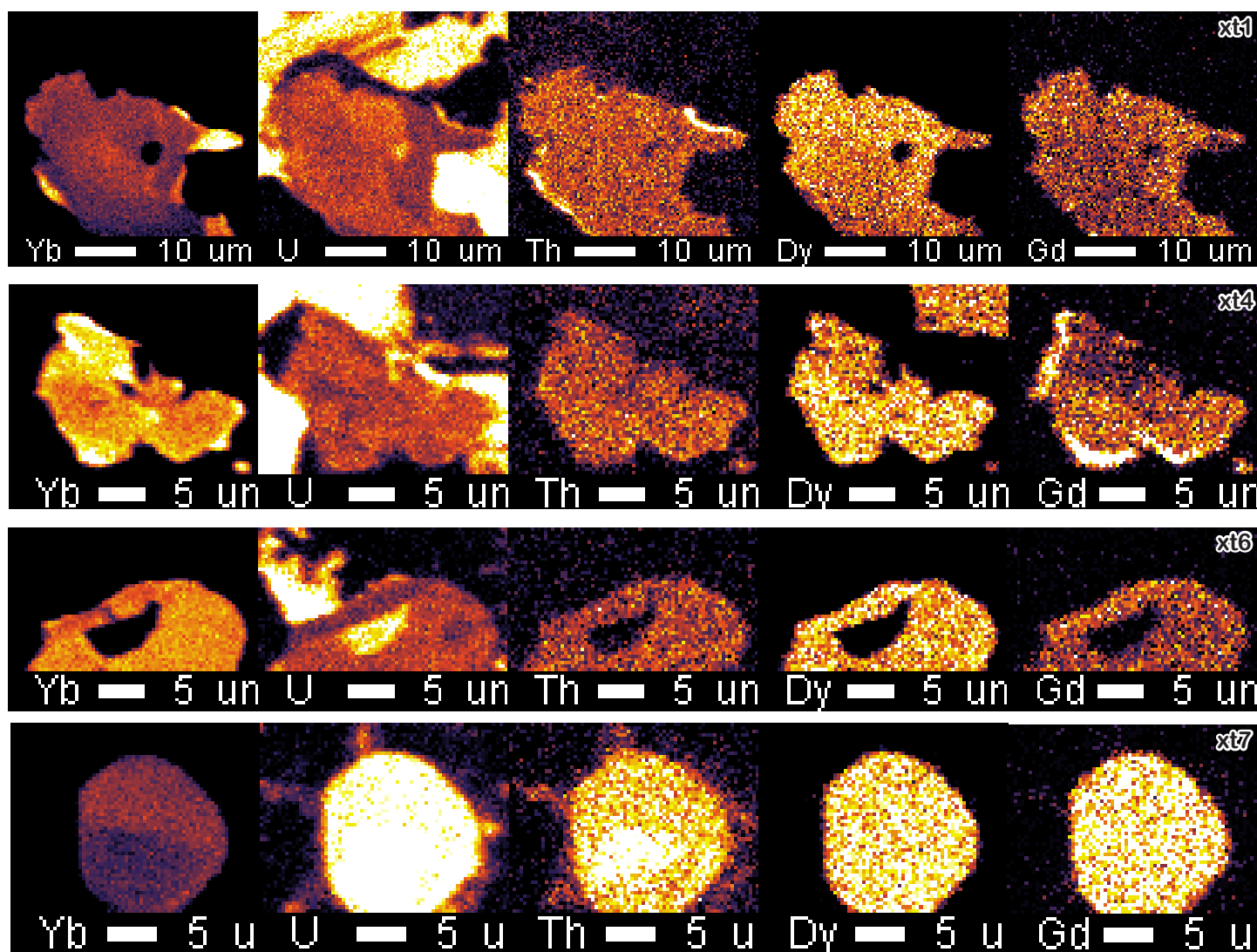


Figure S23B: Simultaneously processed xenotime maps (Yb, U, Th, Dy, Gd) for sample 21IWH18.

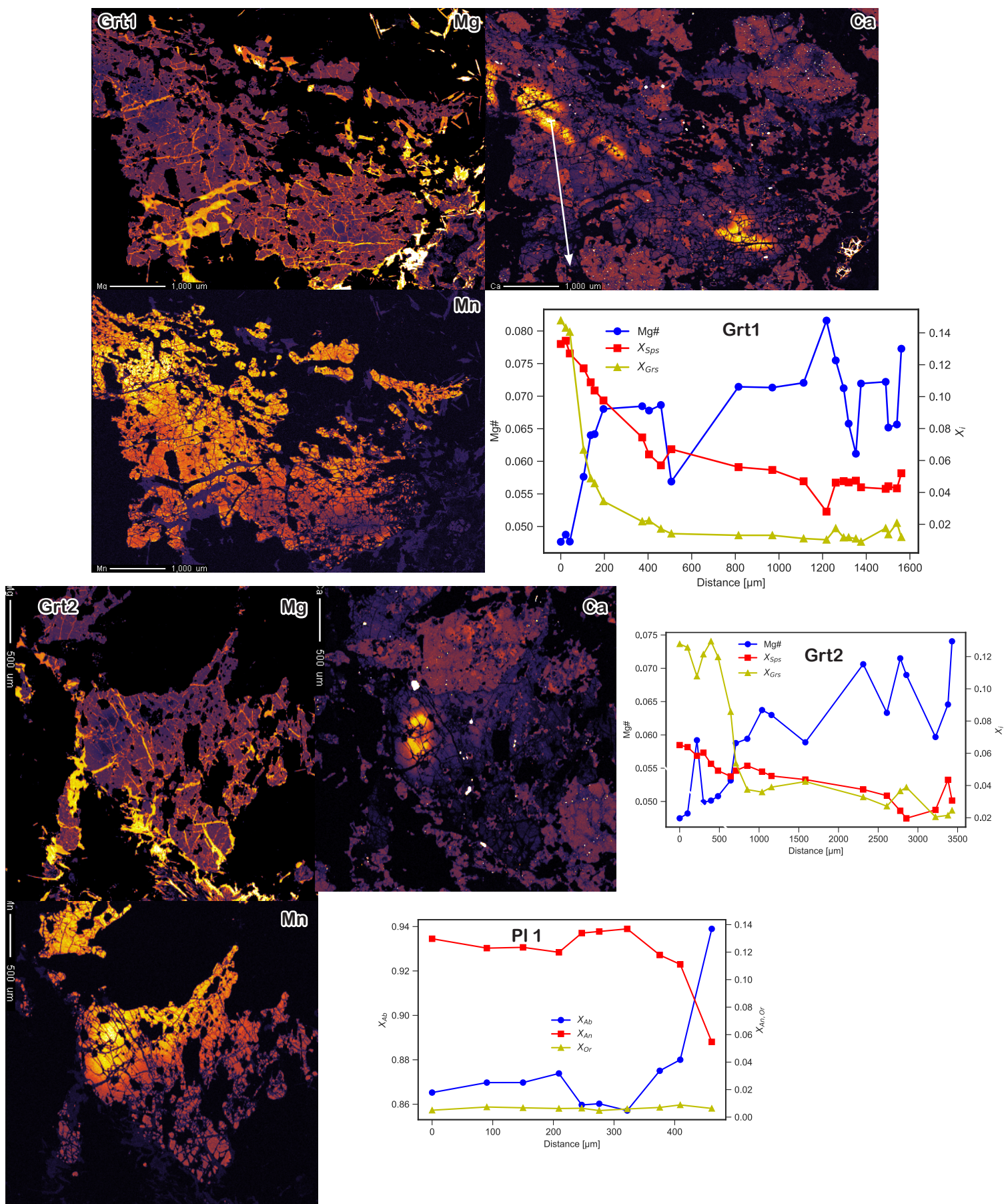


Figure S24. Garnet maps and quantitative transects of garnet and plagioclase from sample 21IWH07.

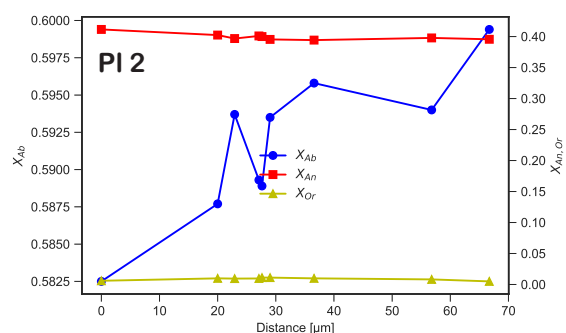
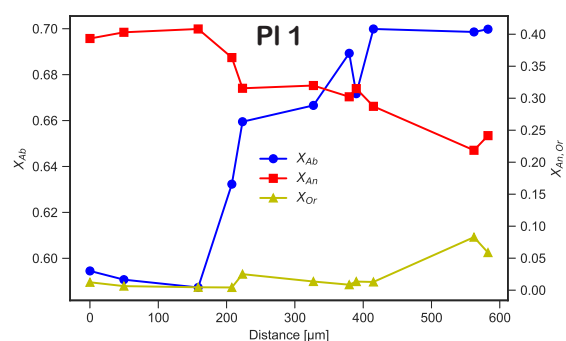
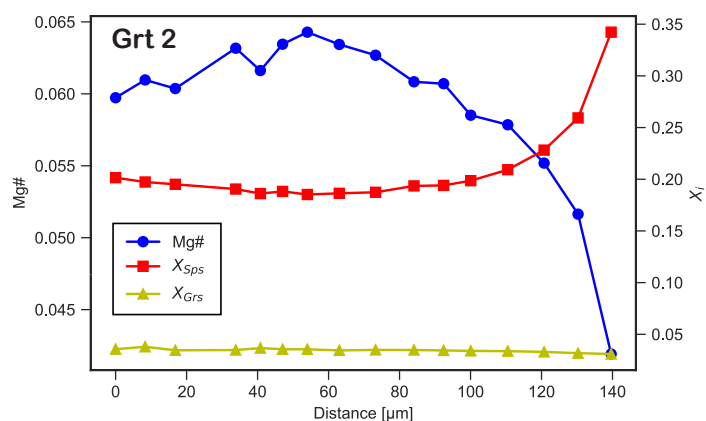
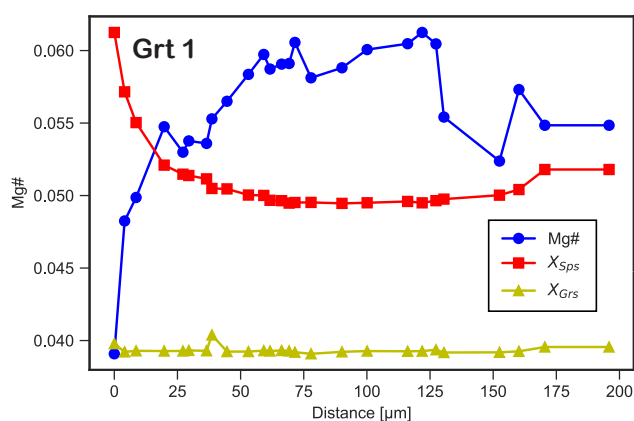
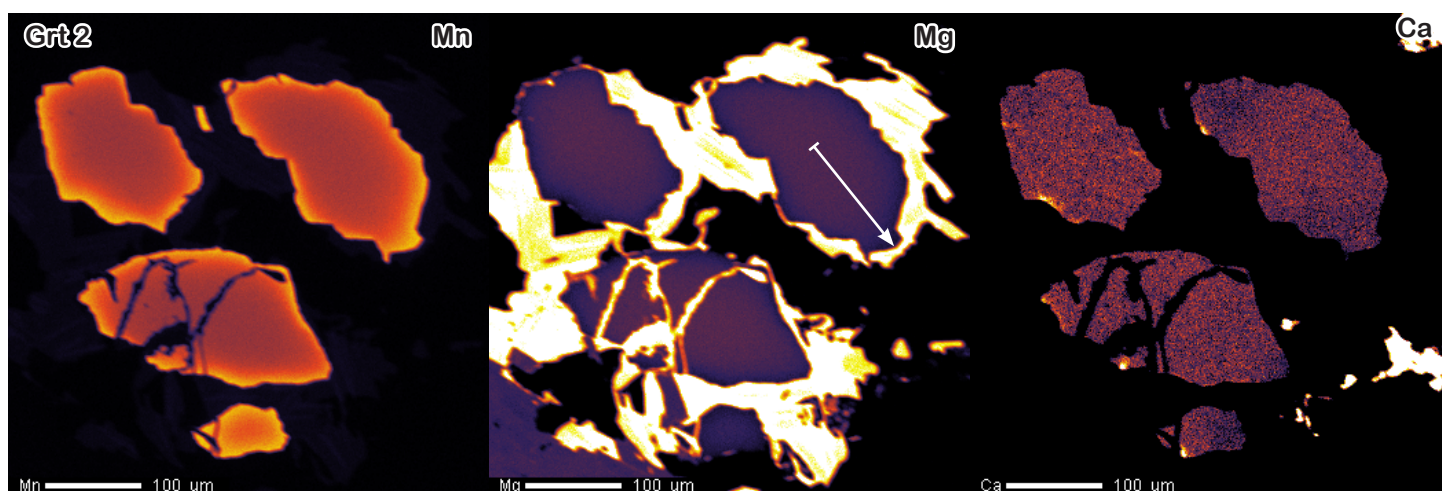
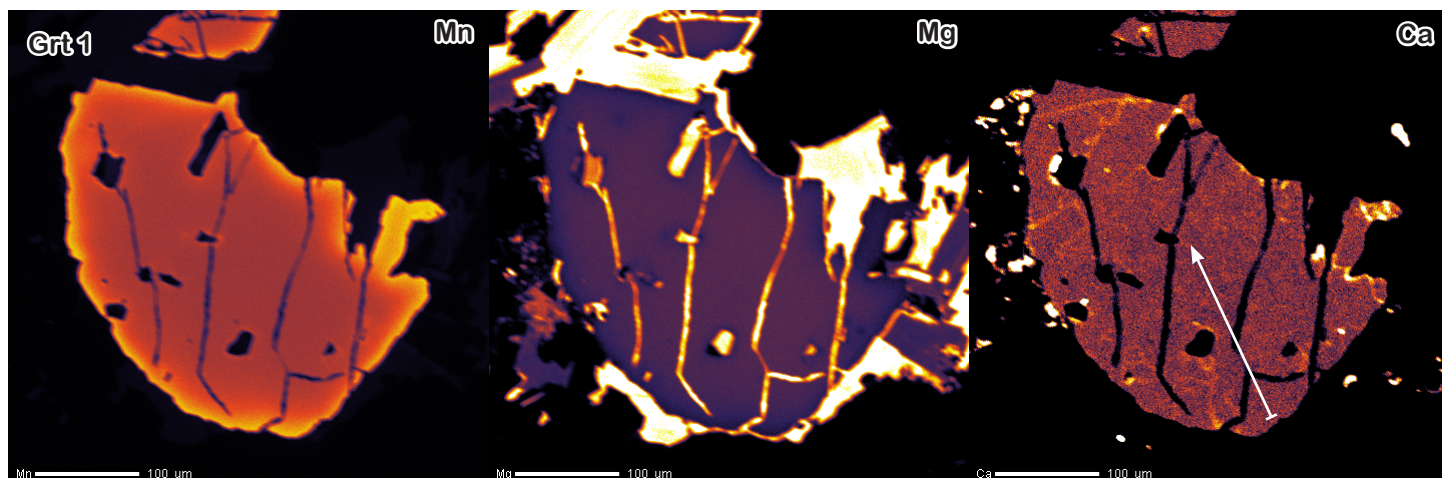


Figure S25. Garnet maps and garnet and plagioclase quantitative transects from sample 21IWH18.

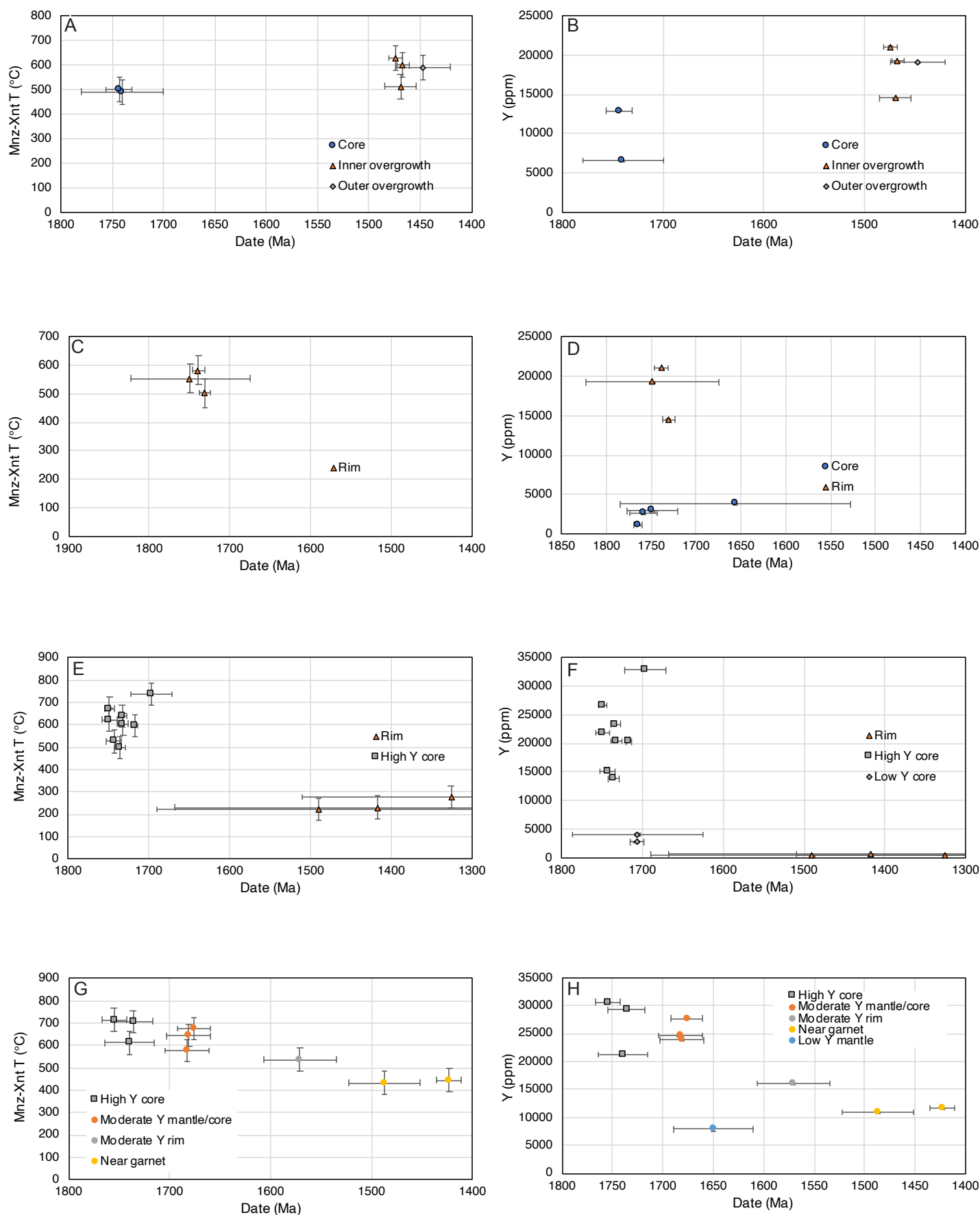


Figure S26: Monazite Y and Th/U vs date for individual compositional domains from samples 21IWH05 (A-B), 21IWH07 (C-D), 21IWH11 (E-F), and 21IWH18 (G-H).

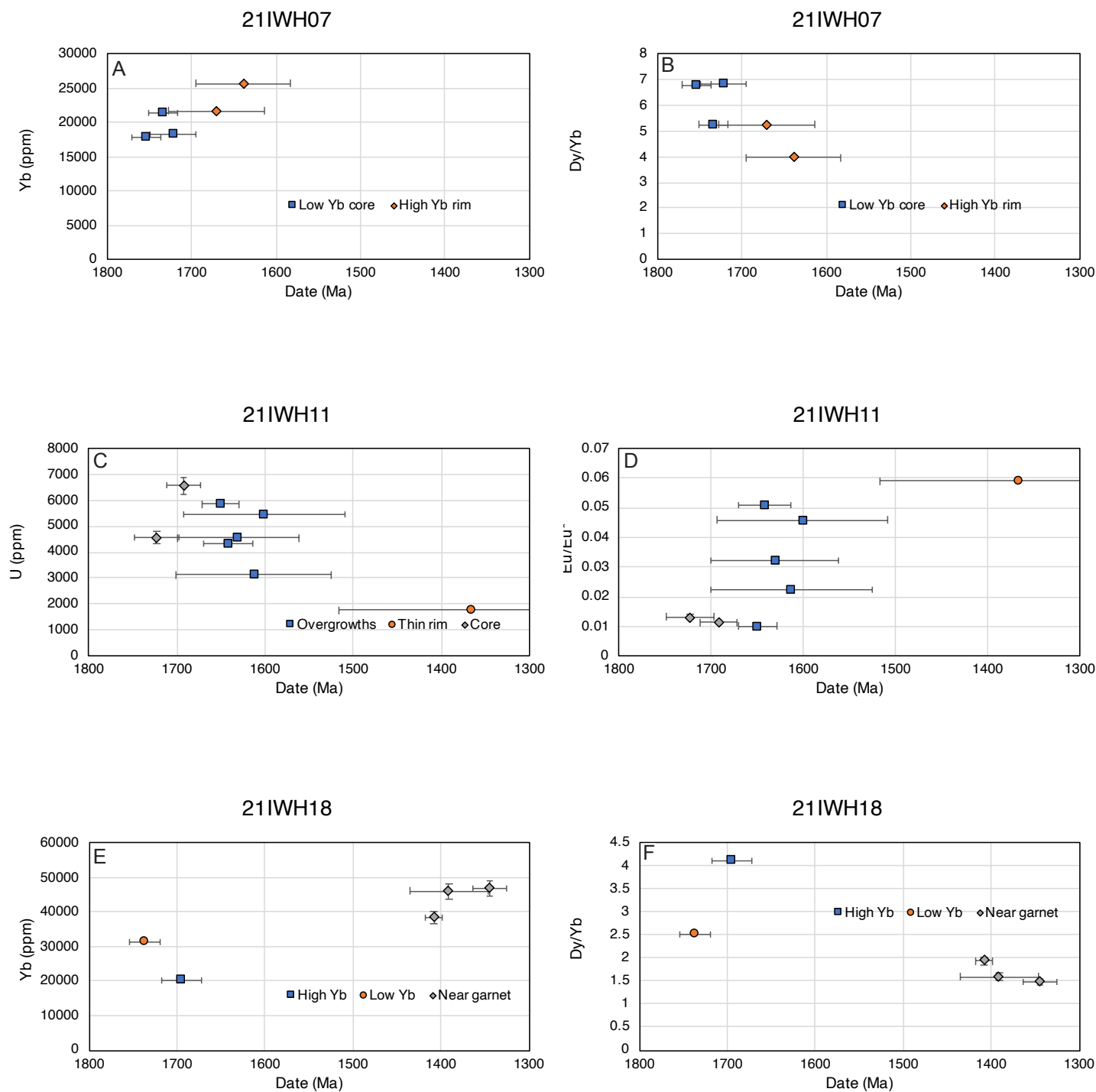


Figure S27: Xenotime trace/rare earth element geochemistry vs. U-Th-Pb_{total} date for individual compositional domains. Points are symbolized by domain type. A: Yb (ppm) vs date in sample 21IWH07. B: Dy/Yb vs date in sample 21IWH07. C: U vs date in sample 21IWH11. D: Eu/Eu* vs date in sample 21IWH11. E: Yb vs date in sample 21IWH18. F: Dy/Yb vs date in sample 21IWH18.

21IWH07

Oxides: H₂O Na₂O MgO Al₂O₃ SiO₂ K₂O CaO FeO TiO₂ MnO

X₀/Mol: 5.5 3.71 2.93 8.04 73.39 .82 68.4 63 .2 .09

Created using GeoPS v3.3.8359.19692

By ihillenbrand at 11/22/2022 9:33:08 AM, Elapsed 00:06:58

Citation: Xiang et al., 2021 JMG

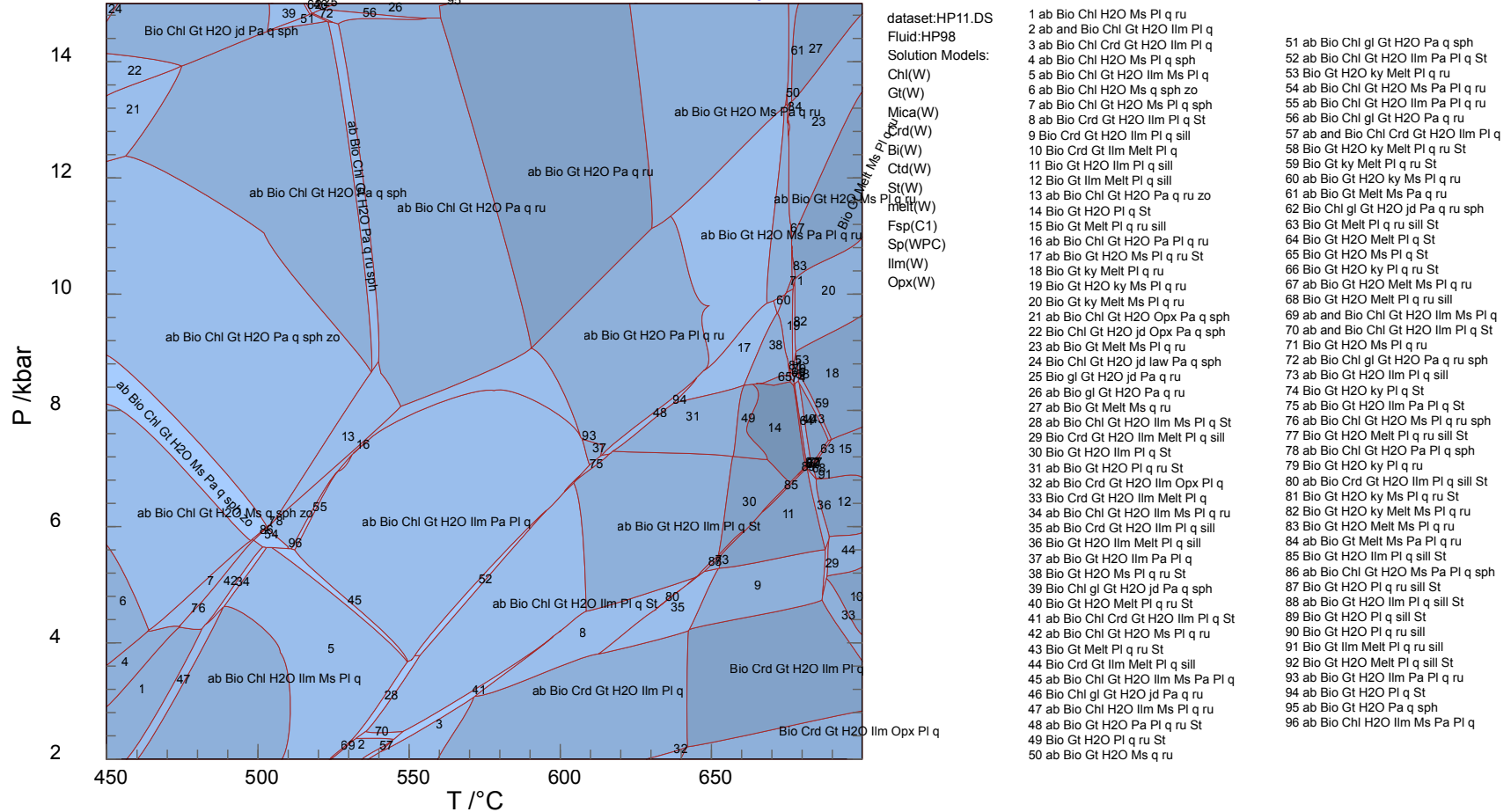


Figure S28: Full isochemical phase diagram (pseudosection) for sample 21IWH07. Figure shows all mineral assemblage stability fields predicted by GeoPs between 450°C and 700°C and 0.2-1.5 GPa. Details regarding bulk composition (adapted from XRF composition), dataset, and activity-solution models are shown on the diagram.

Oxides: H₂O Na₂O MgO Al₂O₃ SiO₂ K₂O CaO FeO TiO₂ MnO
XO/Mol: 3.46 2.94 2.86 7.68 75.07 1.61 1.92 4.12 .22 .11

Created using GeoPS v3.3.8359.19692
By ihillenbrand at 11/21/2022 10:45:13 AM, Elapsed 00:09:17
[Citation: Xiang et al., 2021 JMG](#)

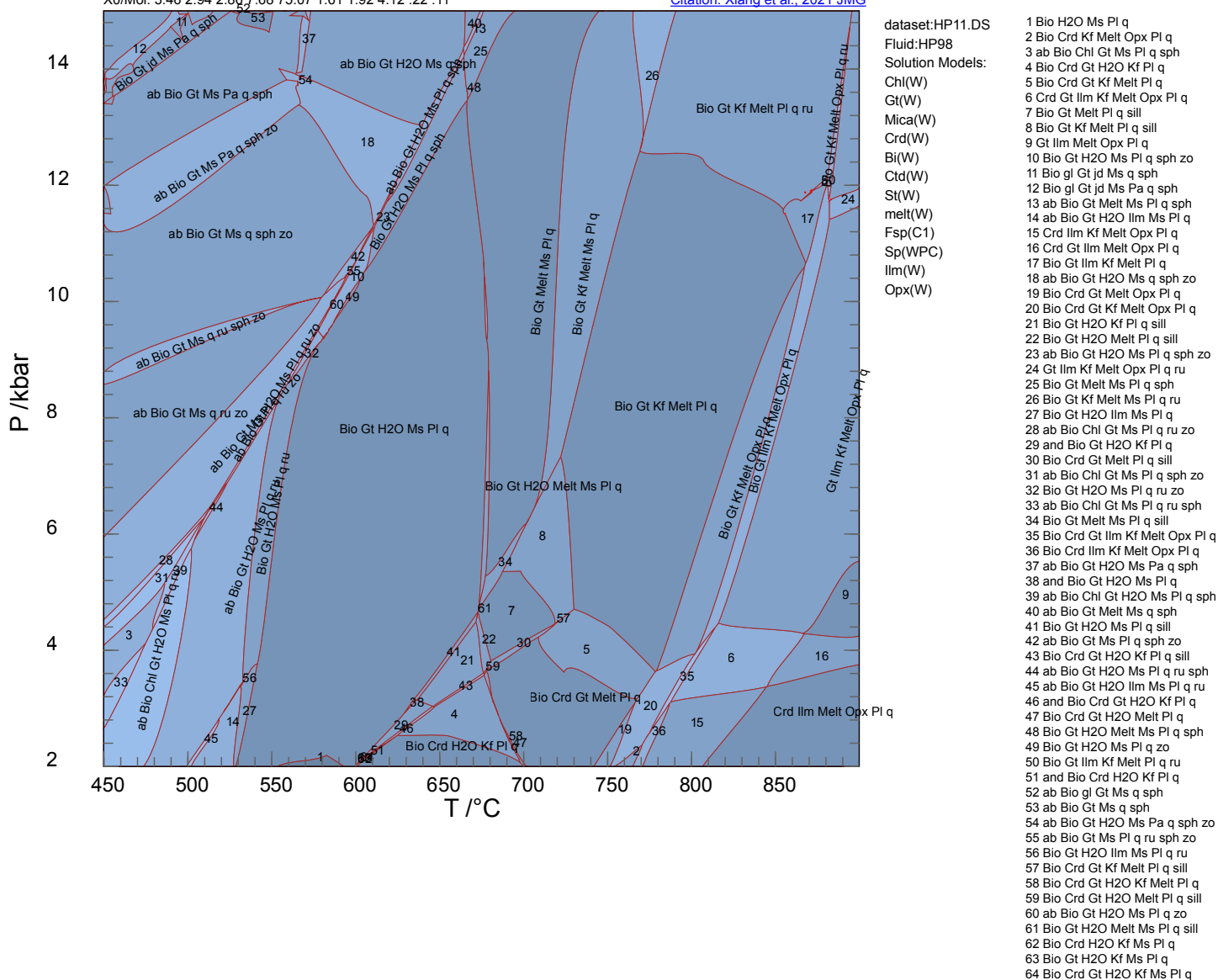


Figure S29: Full isochemical phase diagram (pseudosection) for sample 21IWH18. Figure shows all mineral assemblage stability fields predicted by GeoPs between 450°C and 900°C and 0.2-1.5 GPa. Details regarding bulk composition (adapted from XRF composition), dataset, and activity-solution models are shown on the diagram.



Figure S30: Cathodoluminescence (CL) images for zircon grains from sample 21AG06. LA-ICP-MS spots are shown with white circles and labeled by analysis number. $^{207}\text{Pb}/^{206}\text{Pb}$ dates are noted for analyses passing concordance filters described in the main text.

250 μm

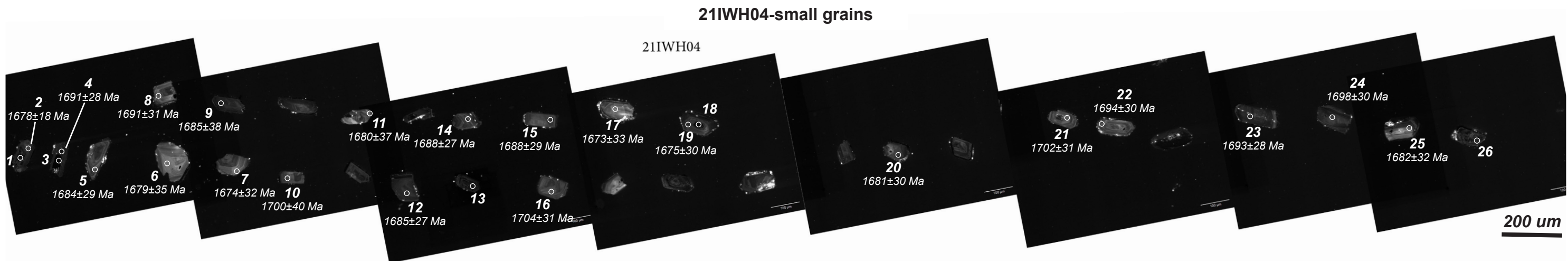
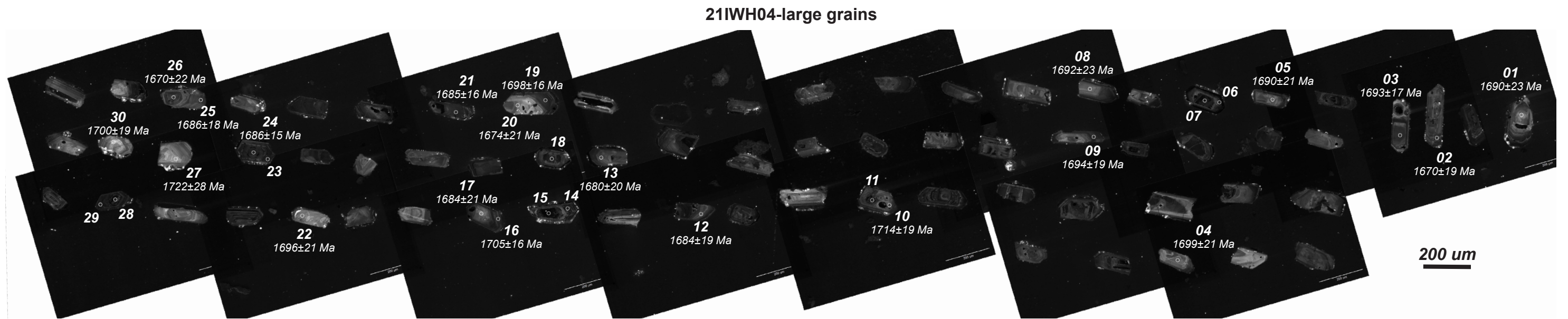


Figure S32: Cathodoluminescence (CL) images for zircon grains from sample 21IWH04. LA-ICP-MS spots are shown with white circles and labeled by analysis number. $^{207}\text{Pb}/^{206}\text{Pb}$ dates are noted for analyses passing concordance filters described in the main text. Two size populations of zircon were mounted; relative large grains are shown in the top row and relatively small grains in the lower row. Both size populations yielded statistically indistinguishable dates and are hence considered together. Relatively small grains are noted with the suffix “sm” in the supplementary dataset.

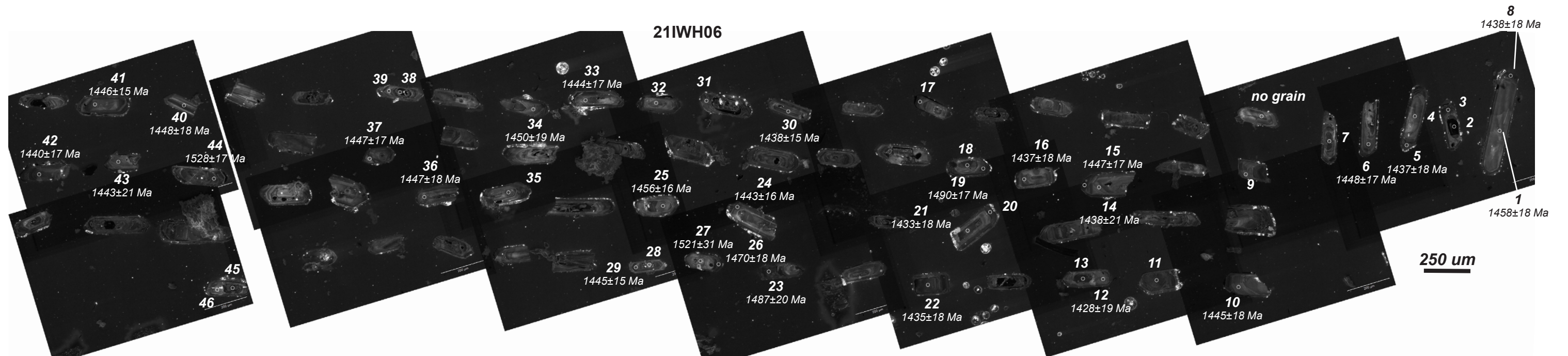


Figure S33: Cathodoluminescence (CL) images for zircon grains from sample 21IWH06. LA-ICP-MS spots are shown with white circles and labeled by analysis number. $^{207}\text{Pb}/^{206}\text{Pb}$ dates are noted for analyses passing concordance filters described in the main text.